Modeling and experimental characterization of squeeze film effects in nonlinear capacitive circular microplates

Aymen Jallouli[a], Najib Kacem[a,*], Fehmi Najar[b], Gilles Bourbon[a], Joseph Lardies[a]

[a] *Univ. Bourgogne Franche-Comté, FEMTO-ST Institute, UMR 6174, CNRS/UFC/ENSMM/UTBM, Department of Applied Mechanics, F-25000, Besançon, France*
[b] *Applied Mechanics and Systems Research Laboratory, Tunisia Polytechnic School, University of Carthage, B.P. 743, La Marsa 2078, Tunisia*

Abstract

In this article, an original approach to model the squeeze film effects in capacitive circular microplates is developed. The nonlinear von Kármán plate theory is used while taking into consideration the electrostatic and geometric nonlinearities of the clamped edge microplate. The fluid underneath the plate is modeled using the nonlinear Reynolds equation with a corrected effective dynamic viscosity due to size effect. The strongly coupled system of equations is solved using the Differential Quadrature Method (DQM) by discretizing the structural and the fluid domains into a set of grid points.
The linear effects of the squeeze film on the microplate have been investigated based on the complex eigenfrequencies of the multiphysical problem. It is shown that the air film can alter the resonance frequencies by adding stiffness as well as damping to the system. The model has been validated numerically with respect to a Finite Element Model (FEM) implemented in ANSYS and experimentally on a fabricated circular microplates.
The nonlinear effects of the squeeze film have been studied by determining the steady state solution of the system using the finite difference method (FDM) coupled with the arclength continuation technique. It is shown that the decrease of the static pressure shifts the resonance frequency and leads to an increase of the vibration amplitude due to the reduction of the damping coefficient, while the increase in the pressure enlarges the bistability domain. The developed model can be exploited as an effective tool to predict the nonlinear dynamic behavior of microplates under the effect of air film for the design of Capacitive Micromachined Ultrasonic Transducers (CMUTs).

Keywords: Squeeze film effects, circular microplates, von Kármán plate theory, Reynolds equation, nonlinear dynamics, differential quadrature method

*Corresponding author. Tel.: +33 3 81 66 67 02; fax: +33 3 81 66 67 00.
Email address: najib.kacem@femto-st.fr (Najib Kacem)

Preprint submitted to Mechanical Systems and Signal Processing

Nomenclature

n	number of grid point	$P(r,t)$	net pressure
λ_a	atmospheric mean free path	P_a	ambient pressure
H	thickness of fluid film	w_j	out-of-plane displacement at $r = r_i$
E	Youngs modulus	u_j	in-plane displacement at $r = r_i$
ρ	density	P_j	net pressure at $r = r_i$
ν	Poisson's ratio	r_i	position of the i^{th} grid points
R	radius of the microplate	H_i	thickness of fluid film at $r = r_i$
R_e	radius of the electrode	Γ_i	geometric nonlinear term at $r = r_i$
d	gap distance	ϕ_i	shape functions of the microplate
d_e	thickness of the electrode	φ_i	shape functions of the fluid pressure
N_0	residual stress	λ_i	i^{th} eigenvalues of the system
ϵ_0	permittivity of the air	ω_i	resonance frequency of the i^{th} mode
η	viscosity	ξ_i	damping coefficient of the i^{th} mode
$V(t)$	electric voltage	M	mass matrices
V_{dc}	static electric voltage	C	damping matrices
V_{ac}	harmonic electric voltage	K	stiffness matrices
ω	excitation frequency	K_{NL}	nonlinear stiffness vector
D	plate flexural rigidity	T_p	period of a solution
Γ	geometric nonlinear term	N_p	number time segment in a period
η_{eff}	effective fluid viscosity	P_i^k	net pressure at $r = r_i$ and $t = k/N_p$
K_n	Knudsen number	$*_{,r}$; $*_{,rr}$	first and second derivative with respect to r
λ_0	molecular mean free path	$\dot{*}$; $\ddot{*}$	first and second derivative with respect to t
w	out-of-plane displacement	u	in-plane displacement
$P_T(r,t)$	total pressure	$A_{ij}^{(k)}$	DQM weighting coefficients of the
h	thickness of the microplate		k^{th} order derivative
σ	squeeze number	w_i^k	out-of-plane displacement at $r = r_i$
P_0	local pressure of the medium		and $t = k/N_p$

1. Introduction

The surrounding fluid has an important impact on the dynamic behavior of resonant microelectromechanical systems (MEMS). For capacitive microdevices, the distance between the two electrodes is relatively small compared to the lateral dimension. The vibration of one of these electrodes can lead to a massive movement of the fluid underneath it. For macrodevices, the effect of surrounding fluid can be negligible compared to other forces, such as inertia and gravity forces. However, for microdevices, the fluid film effects increase as we decrease the system size [1]. The squeeze film effect is one of the most important phenomena which affects the dynamic behavior of resonant MEMS, since it shifts the resonance frequencies (the shift can reach up to 60% of the natural frequency in vacuum [2]) and it adds damping to the system.

The squeeze film effects are in general governed by the Reynolds equation, which describes the pressure distribution of a thin viscous fluid. In 1886, Osborne Reynolds formulated this equation for fluid lubrication applications [3]. The equation was reformulated in its general form by Tipei in 1954 [4] to study the effect of a fluid on two coaxial disks by supposing that there is no slip between fluid particles and moving surfaces. However, when the gap distance of the microsystem is comparable to the mean free path of the fluid, the tangential velocity of the fluid at the boundary cannot be approximated to zero. Therefore, this assumption (no slip between fluid particles and surfaces) is no longer valid [5]. In general, there are four flow regimes: continuum regime, transition regime, slip-flow regime and molecular regime. Each of these regimes are defined using the so called Knudsen number which is given by:

$$K_n = \frac{\lambda_0}{H} \tag{1}$$

where λ_0 is the molecular mean free path of the fluid and H is the thickness of fluid film. Several studies showed that the validity region of the Reynolds equation can be extended by choosing an effective gap distance [6, 7, 8, 9] and the most used one is the model of Veijola *et al.* [10, 11] because it is accurate and valid for a wide range of K_n. Schrag *et al.* [12] performed numerical comparison between the modified Reynolds equation with the results obtained using the Navier-Stokes model. The two models showed a good agreement for different width-to-fluid film thickness. The use of Reynolds equation provides a notable reduction of the computational time compared to the Navier-Stokes model. Also it can be used for complex microsystems like perforated accelerometers [12, 13] magnetometers[14] and micromirrors [15, 16].

Other approaches have been used to model the squeeze film effect in microsystems by determining the quality factor of the resonator. Kadar *et al.* [17] and Li *et al.* [18] developed a model for the computation of the damping parameters of a vibrating microstructure operating in low pressure conditions based on Christian model [19]. The presented models take into consideration the coupling effect between the intrinsic damping and the impact of molecules in high vaccum. The problem with this type of models is that the quality factor is independent of the dimension of the microsystem and the distance between the two plates. Bao *et al.* [20] determined the quality factor of the system by determining the energy losses from the oscillating plate to the surrounding air. It was shown that, for a rectangular microplate the quality factor is proportional to the gap distance and inversely proportional to the plate length and air pressure.

Another method to investigate the effect of the squeeze film on a microsystem consists in approximating the pressure distribution as a nonlinear damping force [21, 22]. Sedighi *et al.* [23] used this method to study the nonlinear dynamic response of a double-sided electromechanical nano-bridge. The increase in the damping coefficient leads to an increase of the dynamic pull-in of the system. However, this model is valid only for an incompressible fluid. That means the stiffness effect is negligible compared to the damping force [24].

The most used technique to study the effect of a surrounding fluid on microsystems is the finite element method (FEM). Chaterjee *et al.* [25] used the modal projection method implemented in ANSYS to determine the stiffness and modal damping coefficients of a cantilever.

The effect of the DC voltage was investigated at different pressures and it was shown that the static pressure can shift the resonance frequency of microsystems and increases the damping forces. FEM models are very efficient especially for systems with complicated shapes like perforated plates [26, 27, 28, 29]. However, this type of model is computationally very time consuming, making it difficult to use when a large number of simulations are needed.

To reduce the computational time, Veijola [10] presented an equivalent-circuit model of a capacitive accelerometer. This model was used to determine the effective viscosity parameter in a narrow gap between the moving surfaces that is valid for viscous and molecular regime.

The solving of a coupled multiphysical system can be also performed by developing a reduced order model. Galerkin method is commonly used for such type of systems to separate the time variable from the space variables by writing the unknown variables as a sum of shape functions and their generalized coordinates. Younis *et al.* [30, 31] used the perturbation method to calculate the displacement and the pressure distributions of flexible microstructures. The model was used to determine an analytical expression of the damping coefficient and the natural frequency of the coupled problem. The obtained results have been compared with the experimental data obtained by Legtenberg and Tilmans [32] and they were in a good agreement. This technique has been used to investigate the effect of the squeeze film on the nonlinear dynamic behavior of MEMS [33].

Capacitive micromachined ultrasonic transducer (CMUT) is one of the most famous microsystems that have been developed in the last decades. It consists of a microplate that vibrate to emit or detect ultrasounds. Several models have been developed to investigate the nonlinear behavior of such systems. Vogl *et al.* [34, 35] developed an analytical model for a circular CMUT based on nonlinear von kármán plate theory. The model is used to investigate the nonlinear frequency and force response of the microplate around the primary resonance frequency. The static and dynamic behavior is very sensitive to residual stress, initial imperfection and squeeze film damping [36, 37, 38, 39]. Galisultanov *et al.* [40] developed a 1D equivalent system, based on a rigid piston model, and a 2D FEM model using COMSOL. The model demonstrates the competition between the electrostatic softening, caused by the DC voltage, and the squeeze film stiffening due to the gap change.

In this paper, we propose a new approach that can be used to investigate the squeeze film effects in capacitive micromachined ultrasonic transducers (CMUTs) based on clamped circular microplates. The behavior of a CMUT is modeled with mechanical equations that takes into consideration the effect of residual stress, electrostatic nonlinearities and geometric nonlinearities. The trapped air between the two electrodes is modeled using the Reynolds equation with an effective viscosity using the Veijola model [10]. The discretization of the coupled partial differential equations is performed using the Differential Quadrature Method (DQM) for the structural and fluid domains. The advantage of this method is that it takes only few grid points for the solution to converge [41, 42]. A first validation is conducted on our model using ANSYS software. For low squeeze number the two numerical results, obtained with DQM and ANSYS, are in a good agreement. However, when the squeeze number is high, the error between the two models increases. Another validation is performed between the experimental and numerical results by taking into account the thickness of the electrode. The nonlinear dynamic behavior of the CMUT is studied by

solving the nonlinear differential equations using FDM in order to determine the steady state solution of the microplate. For the nonlinear frequency response of the CMUT, we modeled the microsystem with a clamped boundary condition for the microplate and with an open boundary condition for the fluid. The decrease in the static pressure in the gap leads to a decrease in the resonance frequency and an increase in the vibration amplitude. At atmospheric conditions, the nonlinear frequency response of the CMUT is obtained by applying high DC and AC voltages. The increase in the static pressure leads to an increase in the bistability domain of the force response curves.

2. Mathematical Model

We consider a flat circular microplate with a uniform cross-section h and a homogeneous material with a density ρ and a Young's modulus E, as shown in Figure 1. The vibrating electrode is modeled as a perfectly clamped circular microplate with radius R excited with an electric voltage $V(t) = V_{dc} + V_{ac}\ cos(\omega t)$ where:

- V_{dc} is the static electric voltage.
- V_{ac} is the amplitude of the harmonic voltage.

The bottom electrode, with radius R_e and thickness d_e, is placed below the microplate at a distance d.

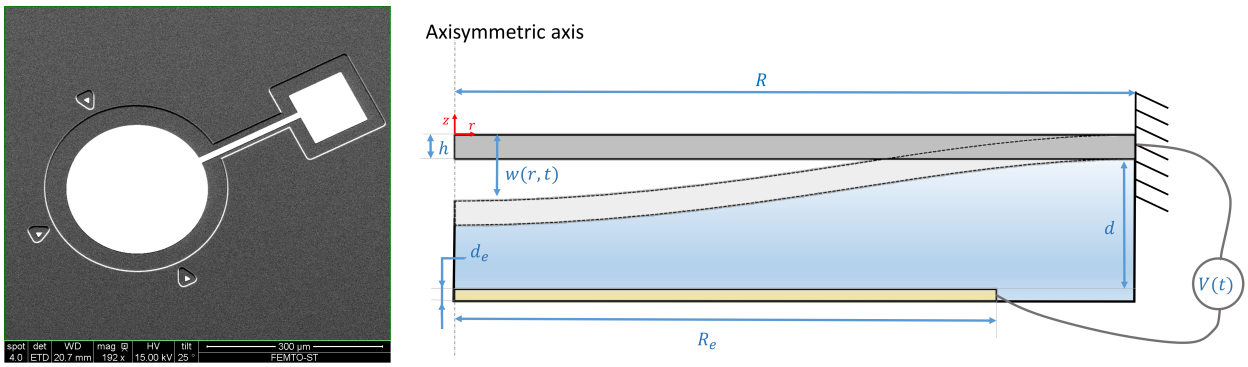

Figure 1: (a) A scanning electron microscope photo of a CMUT before bonding the upper microplate to the substrate. (b) A cross section of a circular electrostatic thin microplate.

2.1. Governing equations of motion

The microplate equations of motion are derived from the nonlinear von Kármán plate theory. We consider the following hypothesis [43]:

- A straight line (filament), initially normal to the midplane, remains straight and normal to the surface during the deformation.
- The stress normal to the midplane, σ_z, is small compared to the other stress components and may be neglected in the stress-strain relations.

The partial differential equations that describe the vibration of a clamped circular plate are given by [39]:

$$\rho h\ddot{w} + c\dot{w} + D\nabla^4 w = N_0\left(\frac{1}{r}w_{,r} + w_{,rr}\right) + \frac{\epsilon_0 V^2(t)}{2(d-w)^2} - P(r,t)$$
$$+ \frac{12D}{h^2}\left[\frac{1}{r}u_{,r}w_{,r} + u_{,rr}w_{,r} + u_{,r}w_{,rr} + \frac{1}{2r}(w_{,r})^3 + \frac{3}{2}(w_{,r})^2 w_{,rr} + \frac{\nu}{r}\left(u_{,r}w_{,r} + uw_{,rr}\right)\right] \quad (2)$$

$$u_{,rr} + \frac{1}{r}u_{,r} - \frac{u}{r^2} = -\frac{1-\nu}{2r}(w_{,r})^2 - w_{,r}w_{,rr} \quad (3)$$

where w and u represent the out-of-plane and in-plane displacement of the microplate and $P(r,t)$ represents the external forces applied on the microplate. $w_{,r}, u_{,r}$ and $w_{,rr}, u_{,rr}$ are the first and second derivative of w and u with respect to r. $\nabla^4 = \left(\frac{\partial^2}{\partial r^2} + \frac{1}{r}\frac{\partial}{\partial r}\right)^2$ is the bi-harmonic operator, $D = \frac{Eh^3}{12(1-\nu^2)}$ is the plate flexural rigidity, ϵ_0 is the vacuum permittivity, N_0 is the residual stress and ν is the Poisson's ratio.

For an axisymmetric problem, the microplate has always a horizontal tangent at $r = 0$ and the in-plane displacement is equal to zero $u = 0$. The boundary conditions of the clamped circular microplate are:

$$\begin{array}{lll} \text{At } \ r = 0: & w_{,r} = 0 & u = 0 \\ \text{At } \ r = R: & w_{,r} = w = 0 & u = 0 \end{array} \quad (4)$$

To describe the effects of a thin layer of fluid between the moving plate and the fixed electrode, we use the Reynolds equation. This equation is derived from the Navier-Stokes equation based on these assumptions:

(i) The fluid is Newtonian.

(ii) The flow is laminar.

(iii) The fluid obeys the ideal gas law.

(iv) No slip between fluid particles and surfaces.

(v) Negligible fluid inertia compared to the viscous and pressure forces (small Reynolds number).

(vi) The thickness of the film is small compared to the radius of the plate $\beta = \frac{d}{R} << 1$.

(vii) The heating effects are negligible.

Assuming an axisymmetric pressure distribution, the pressure component is determined by solving the following Reynolds equation of a fluid between two circular plates:

$$\frac{\partial}{\partial r}\left(rH^3P_T\frac{\partial P_T}{\partial r}\right) = 12\eta r\left(H\frac{\partial P_T}{\partial t} + P_T\frac{\partial H}{\partial t}\right) \tag{5}$$

where η is the viscosity coefficient of the fluid, H is the total gap distance between the two plates and P_T represents the total pressure in the gap, which is defined as:

$$P_T = P_0 + P(r,t) \tag{6}$$

and P_0 is the local pressure of the medium. In this case, we suppose that the static pressure is applied on both upper and lower surfaces of the microplate. Therefore, The resultant external forces applied on the microplate are equal to the dynamic quantity of pressure $P(r,t)$. For the pressure boundary conditions, we suppose that the fluid is trapped inside the gap. Therefore, the flux at the clamped edge is equal to zero. Hence, the derivative of P_T with respect to r is also zero at $r = R$. At the center of the plate, the pressure is maximum which means that the derivative of P_T with respect to r is zero at $r = 0$. Hence, the boundary conditions of a circular plate are defined as:

$$\left.\frac{\partial P_T}{\partial r}\right|_{r=0} = \left.\frac{\partial P_T}{\partial r}\right|_{r=R} = 0 \tag{7}$$

When the gap distance of the microsystem is comparable to the mean free path of the fluid, the tangential velocity of the fluid at the boundary cannot be approximated to zero. Many studies have been carried out on the effective viscosity and the most used one is the model of Veijola *et al.* [10] because it is accurate and valid for a large range of K_n. The effective viscosity described in the Veijola model is given by [10]:

$$\eta_{eff} = \frac{\eta}{1 + 9.638K_n^{1.159}} \qquad \text{where} \qquad K_n = \frac{P_a\lambda_a}{P_0H} \tag{8}$$

η_{eff} is the effective fluid viscosity in the gap that replaces the actual fluid viscosity η to extend the validity region of the Reynolds equation especially when the Knudsen number is close to the noncontinuum regime. P_a and λ_a are the pressure and the molecular mean free path in ambient condition. The total gap distance H between the two plates is defined as:

$$H = d_t(r) - w(r,t) \tag{9}$$

where $d_t(r)$ is the gap distance defined as:

$$d_t(r) = \begin{cases} d & r \leq R_e \\ d + d_e & r > R_e \end{cases} \tag{10}$$

where d_e is the electrode thickness as it is shown in Figure 1.

2.2. Nondimensional equations of motion

In order to reduce the complexity of the physical parameters, we rewrite equations (2), (3) and (5) in terms of nondimensional variables, which are defined as follows:

$$\begin{aligned}
&r = R\tilde{r}; && u = d\tilde{u}; && w = d\tilde{w} \\
&c = \frac{(D\rho h)^{1/2}}{R^2}\tilde{c}; && \gamma = \frac{12Rd}{h^2}; && \beta = \frac{d}{R} \\
&N_0 = \frac{D}{R^2}\tilde{N}_0; && t = T\tilde{t} = R^2\left(\frac{\rho h}{D}\right)^{1/2}\tilde{t}; && \alpha_e = \frac{\varepsilon_0 R^4}{2Dd^3} \\
&P_T = P_0\tilde{P}_T = P_0(1+P); && H = d\tilde{H} && P_{ND} = \frac{R^4 P_0}{Dd};
\end{aligned} \tag{11}$$

Substituting (11) into (2),(3) and (5) and dropping the tilde ($\sim$) in the result, we get:

$$\ddot{w} + c\dot{w} + \nabla^4 w = N_0\left(\frac{1}{r}w_{,r} + w_{,rr}\right) + \alpha_e\frac{V^2(t)}{(1-w)^2} - P_{ND}P + \gamma\Gamma(w,u) \tag{12}$$

$$u_{,rr} + \frac{1}{r}u_{,r} - \frac{u}{r^2} = -\beta\left(\frac{1-\nu}{2r}(w_{,r})^2 + w_{,r}w_{,rr}\right) \tag{13}$$

$$\frac{\partial}{\partial r}\left(rH^3P_T\frac{\partial P_T}{\partial r}\right) = \sigma r\left(H\frac{\partial P_T}{\partial t} + P_T\frac{\partial H}{\partial t}\right) \tag{14}$$

where Γ is defined as:

$$\Gamma(w,u) = \frac{1}{r}u_{,r}w_{,r} + u_{,rr}w_{,r} + u_{,r}w_{,rr} + \beta\left(\frac{1}{2r}(w_{,r})^3 + \frac{3}{2}(w_{,r})^2 w_{,rr}\right) + \frac{\nu}{r}(u_{,r}w_{,r} + uw_{,rr}) \tag{15}$$

where $\sigma = \frac{12\eta_{eff}R^2}{d^2P_0T}$ represents the squeeze number [44], which refers to the compressibility of the fluid in the gap. For a small value of σ, the compressibility effect can be neglected and the fluid can be considered as incompressible. However, for a higher value of σ, the air is trapped inside the gap and acts as a spring.

For convenience, we rewrite the boundary conditions (4) and (7) in their nondimensional form:

$$\begin{aligned}
&\text{At}\ \ r = 0: && w_{,r} = 0 && u = 0 && \frac{\partial P_T}{\partial r} = 0 \\
&\text{At}\ \ r = 1: && w_{,r} = w = 0 && u = 0 && \frac{\partial P_T}{\partial r} = 0
\end{aligned} \tag{16}$$

3. Discretization

3.1. Differential quadrature method (DQM)

In order to solve the equations of motion of the system, we reduce the partial differential equations (PDEs) into a finite ordinary differential equations (ODEs). One of the methods that has been used in the literature for microscale structures is the DQM [41, 42]. The aim of this method is to discretize the space domain into a grid of sampling points and approximating the derivative with respect to r as a weighted sum of the function at the grid points. The derivative of the unknown parameters w, u and P can be expressed as:

$$\left[\frac{\partial^k w}{\partial r^k}\right]_{r=r_i} = \sum_{j=1}^{n} A_{ij}^{(k)} w_j; \qquad \left[\frac{\partial^k u}{\partial r^k}\right]_{r=r_i} = \sum_{j=1}^{n} A_{ij}^{(k)} u_j; \qquad \left[\frac{\partial^k P}{\partial r^k}\right]_{r=r_i} = \sum_{j=1}^{n} A_{ij}^{(k)} P_j \tag{17}$$

where w_j, u_j and P_j are respectively the out-of-plane displacement, in-plane displacement and the net pressure at the grid point $r = r_i$. Where r_i are the grid points defined by Chebyshev-Gauss-Lobatto [45]:

$$r_i = \frac{1}{2}\left(1 - \cos\left(\frac{(i-1)}{(n-1)}\pi\right)\right) \tag{18}$$

$A_{ij}^{(k)}$ are the DQM weighting coefficients of the kth order derivative which are given by [46, 47, 48]:

$$\begin{aligned}
A_{ij}^{(1)} &= \frac{\prod_{v=1;v\neq i}^{n}(r_i - r_v)}{(r_i - r_j)\prod_{v=1;v\neq j}^{n}(r_j - r_v)} && i,j = 1,2,\cdots,n && i \neq j \\
A_{ij}^{(k)} &= k\left(A_{ii}^{(k-1)} A_{ij}^{(1)} - \frac{A_{ij}^{(k-1)}}{(r_i - r_j)}\right) && i,j = 1,2,\cdots,n && i \neq j \\
A_{ii}^{(k)} &= -\sum_{v=1;v\neq i}^{n} A_{iv}^{(k)} && i = 1,2,\cdots,n
\end{aligned} \tag{19}$$

$A_{ij}^{(k)}$ are the respective weighting coefficients that depend only on the sampling points. The advantage of using this configuration is that it can converge only with a few number of grid points. Also, it reduces the computational time as a result of the properties of the weighting matrix $\left[\mathrm{A}^{(k)}\right]$ [49, 50]

3.2. Discretization of the governing equations

The discretized form of the microplate equations coupled with the Reynolds equation can be written as:

$$EQ_w^{dy}(w_i,u_i,P_i):\ddot{w}_i+c\dot{w}_i+\nabla^4 w_i=N_0\left(\frac{1}{r_i}\sum_{j=1}^{n}A_{ij}^{(1)}w_j+\sum_{j=1}^{n}A_{ij}^{(2)}w_j\right)$$
$$+\alpha_e\frac{V^2(t)}{(1-w_i)^2}-P_{ND}P_i+\gamma\Gamma_i(w_j,u_j);\quad i=2,\cdots,n-2 \tag{20}$$

$$EQ_u^{dy}(w_i,u_i):\sum_{j=1}^{n}A_{ij}^{(2)}u_j+\frac{1}{r_i}\sum_{j=1}^{n}A_{ij}^{(1)}u_j-\frac{u_i}{r_i^2}=$$
$$-\beta\left(\frac{1-\nu}{2r_i}\left(\sum_{j=1}^{n}A_{ij}^{(1)}w_j\right)^2+\sum_{j=1}^{n}A_{ij}^{(1)}w_j\sum_{j=1}^{n}A_{ij}^{(2)}w_j\right);\quad i=2,\cdots,n-1 \tag{21}$$

$$EQ_P^{dy}(w_i,P_i):\sum_{j=1}^{n}A_{ij}^{(1)}\left(r_jH_j^3(1+P_j)\sum_{k=1}^{n}A_{jk}^{(1)}P_k\right)=\sigma r_i\left(H_i\dot{P}_i-(1+P_i)\dot{w}_i\right);$$
$$i=2,\cdots,n-1 \tag{22}$$

where

$$\nabla^4 w_i=\left[w_{,rrrr}+\frac{2}{r}w_{,rrr}-\frac{1}{r^2}w_{,rr}+\frac{1}{r^3}w_{,r}\right]_{r=ri}$$
$$=\sum_{j=1}^{n}A_{ij}^{(4)}w_j+\frac{2}{r_i}\sum_{j=1}^{n}A_{ij}^{(3)}w_j-\frac{1}{r_i^2}\sum_{j=1}^{n}A_{ij}^{(2)}w_j+\frac{1}{r_i^3}\sum_{j=1}^{n}A_{ij}^{(1)}w_j \tag{23}$$

and Γ_i is the discrete form of Γ:

$$\Gamma_i(w_j,u_j)=\frac{1}{r_i}\sum_{j=1}^{n}A_{ij}^{(1)}u_j\sum_{j=1}^{n}A_{ij}^{(1)}w_j+\sum_{j=1}^{n}A_{ij}^{(2)}u_j\sum_{j=1}^{n}A_{ij}^{(1)}w_j+\sum_{j=1}^{n}A_{ij}^{(1)}u_j\sum_{j=1}^{n}A_{ij}^{(2)}w_j$$
$$+\beta\left(\frac{1}{2r_i}\left(\sum_{j=1}^{n}A_{ij}^{(1)}w_j\right)^3+\frac{3}{2}\left(\sum_{j=1}^{n}A_{ij}^{(1)}w_j\right)^2\sum_{j=1}^{n}A_{ij}^{(2)}w_j\right)$$
$$+\frac{\nu}{r_i}\left(\sum_{j=1}^{n}A_{ij}^{(1)}u_j\sum_{j=1}^{n}A_{ij}^{(1)}w_j+u_i\sum_{j=1}^{n}A_{ij}^{(2)}w_j\right) \tag{24}$$

H_i is the nondimensional film thickness at the i^{th} grid point defined as:

$$H_i=d_t(r_i)-w_i(t)\qquad\text{where}\qquad d_t(r_i)=\begin{cases}1 & r_i\le\frac{R_e}{R}\\ 1+\frac{d_e}{d} & r_i>\frac{R_e}{R}\end{cases} \tag{25}$$

and the boundary conditions are :

$$\begin{aligned}
&\text{At } \; r=0: && \sum_{j=1}^{n} A_{1j}^{(1)} w_j = 0 && u_1 = 0 && \sum_{j=1}^{n} A_{1j}^{(1)} \bar{P}_j = 0 \\
&\text{At } \; r=1: && \sum_{j=1}^{n} A_{nj}^{(1)} w_j = w_n = 0 && u_n = 0 && \sum_{j=1}^{n} A_{nj}^{(1)} \bar{P}_j = 0
\end{aligned} \tag{26}$$

4. Eigenvalue modeling

4.1. Eigenvalue problem using DQM

In this section, we investigate the effect of the air film on the resonance frequencies and damping coefficients. The system of equations is composed of three nonlinear partial differential equations. The first equation (20) is the equation of motion for the downward displacement w. The second one (21) is the equation that describes the transverse displacement u. The third equation (22) represents the Reynolds equation that couples the displacement of the plate with the pressure in the gap. For n grid points, the total number of equations is equal to $3 \times n$, which increases the computational time. To reduce the number of equations, we write the radial displacement u_i as a function of w_i using equation (21) and we replace the expression of u_i in equation (20). At the boundary nodes, we use equations (26) to determine the boundary displacements $\{w_1, w_{n-1}, w_n\}$ and pressures $\{P_1, P_n\}$. This simplification reduces the total number of equations to $2 \times n - 5$. Then, we decompose the total displacement w_i into a static component w_i^s and a dynamic component w_i^d.

$$w(r = r_i, t) = w_i(t) = w_i^s + w_i^d(t) \tag{27}$$

Substituting the expression of w_i into the Reynolds equation, we obtain:

$$\begin{aligned}
\sum_{j=1}^{n} A_{ij}^{(1)} \left(r_j \big(d_t(r_j) - w_j^s - w_j^d(t)\big)^3 (1 + P_j) \sum_{k=1}^{n} A_{jk}^{(1)} P_k \right) = \\
\sigma r_i \left(\big(d_t(r_i) - w_i^s - w_i^d(t)\big) \dot{P}_i - (1 + P_i)\dot{w}_i \right); \quad i = 2, \cdots, n-1
\end{aligned} \tag{28}$$

The resonance frequencies of the structure and the damping coefficients are determined by solving the damped eigenvalues of the system of equations (20) and (22) which can be written as:

$$M\ddot{Y}(t) + C\dot{Y}(t) + KY(t) + K_{NL}(Y(t), \dot{Y}(t)) = 0 \tag{29}$$

where M, C and K are the mass, damping and stiffness matrices; $K_{NL}(Y(t), \dot{Y}(t))$ is the vector with nonlinear parameters and $Y(t)$ is the vector of unknowns defined as:

$$Y(t) = \left\{ w_2^d, \cdots, w_{n-2}^d, P_2, \cdots, P_{n-1} \right\} \tag{30}$$

where the unknown parameters $\left\{ w_1^d, w_{n-1}^d, {w_n}^d \right\}$ are expressed as a function of w_i^d for $i = 2, \cdots, n-2$ using the boundary conditions (26). Also, for the pressure parameters, we

expressed $\{P_1, P_n\}$ as a function of P_i for $i = 2, \cdots, n-1$ using equations (26). To determine the resonance frequencies and damping coefficients, we neglect the nonlinear part K_{NL}. Even with this approximation, the solving of this type of system (29) remains difficult. Therefore, by following Meirovitch *et al.* [51], we transform equation (29) to the general eigenvalue problem by defining $\chi_1 = Y(t)$ and $\chi_2 = \dot{Y}(t)$:

$$\begin{bmatrix} M & 0 \\ 0 & K \end{bmatrix} \frac{\partial}{\partial t} \begin{bmatrix} \dot{Y} \\ Y \end{bmatrix} = \begin{bmatrix} -C & -K \\ K & 0 \end{bmatrix} \begin{bmatrix} \dot{Y} \\ Y \end{bmatrix} \tag{31}$$

Then, we determine the linear damped eigenvalues and eigenvectors by formulating the harmonic displacement amplitude and pressure as follow:

$$\begin{aligned} w_i^d(t) &= \phi_i e^{j\omega t} \\ P_i(t) &= \varphi_i e^{j\omega t} \end{aligned} \tag{32}$$

where ϕ_i and φ_i are the shape functions of the microplate and fluid pressure associated to the frequency ω at the nodes $r = r_i$. Substituting the expression of w_i and P_i into equation (31), the system of equations becomes:

$$(\lambda A - B)\,\chi = 0 \tag{33}$$

where

$$\lambda = j\omega \qquad A = \begin{bmatrix} M & 0 \\ 0 & K \end{bmatrix} \qquad B = \begin{bmatrix} -C & -K \\ K & 0 \end{bmatrix}$$

$$\chi = \{\lambda Y, Y\} = \left\{\lambda\phi_2^d, \cdots, \lambda\phi_{n-2}^d, \lambda\varphi_2, \cdots, \lambda\varphi_{n-1}, \phi_2^d, \cdots, \phi_{n-2}^d, \varphi_2, \cdots, \varphi_{n-1}\right\} \tag{34}$$

The eigenvalues and eigenvectors are then obtained by solving equation (33). The resonance frequency and the damping parameter of the i$^{\text{th}}$ mode satisfy:

$$\omega_i = \left|\mathrm{Re}\left(-j\lambda_i\right)\right| \qquad \text{and} \qquad \xi_i = \frac{\left|\mathrm{Im}\left(-j\lambda_i\right)\right|}{\left|\mathrm{Re}\left(-j\lambda_i\right)\right|} \tag{35}$$

where Re and Im denote the real and imaginary part, respectively.

To this end, it is important to study the effect of the number of grid points n on the convergence of the solution. In figure 2, we present the convergence of the first three axisymmetric modes with respect to the number of grid points n by solving the system of equations (31). For these simulations, we used the physical parameters of the solid and fluid presented in Table 1, where the residual stress N_0 is determined in order to match the numerical and experimental first two resonance frequencies [52].

The resonance frequencies of the coupled system are determined for a clamped circular microplate at atmospheric conditions. With only 8 grid points, we can determine the first three resonance frequencies of the coupled problem with an error of 6 % for the 3rd mode and less than 1 % for the first two modes. By increasing the number of grid points, the three modes converge and 10 points are sufficient to investigate the eigenvalues of the coupled problem. The error for the first two resonance frequencies is less than 0.04 %. DQM is able to predict the first resonance frequencies of the coupled multiphysical system with only few grid points and a high accuracy.

Table 1: Physical parameters of the CMUT

Symbol	Quantity	Dimension
E	Youngs modulus	149 [GPa]
ρ	Density	2330 [kg/m^3]
ν	Poisson's ratio	0.27
R	Radius of the microplate	116 [μm]
R_e	Radius of the electrode	75 [μm]
h	Thickness of the microplate	2.25 [μm]
d	Gap distance	0.770 [μm]
d_e	Thickness of the electrode	0.3 [μm]
N_0	Residual stress	2.6 [MPa]
ϵ_0	Permittivity of the air	8.85 10^{-12} [F/m]
η	Viscosity	1.83 10^{-5} [Ns/m^2]
λ_a	Atmospheric mean free path	64 [nm]

4.2. Eigenvalue problem using FEM

The squeeze film effects can also be investigated using the finite element method. The damping and stiffness parameters are determined using the modal projection technique implemented in ANSYS. The squeeze film effects are determined by computing the velocity profiles of the structure. The multiphysical problem is solved by coupling two domains: structure and fluid. The structure domain is modeled with SOLID185 used for three-dimensional solid structures. The element has the capability to be implemented with stress stiffening, large deflection, large strain and plasticity effects. For the fluid domain, element FLUID136 is used to model the viscous fluid flow in the small gap separating two surfaces, which is based on linearized Reynold equation, where only linear terms are taken into consideration [53]. The Reynolds equation is defined with an effective viscosity η_{eff} as it was presented by Veijola *et al*. [10] in equation (8). The physical parameters used in the next simulations are listed in Table 1.

As shown in Figure 3, the solid volume is meshed with hexahedral elements while the fluid surface is meshed with quadrilateral elements where the fluid nodes are the same nodes as the lower surface of the solid. After that, the clamped boundary conditions of the plate are defined on the lateral surface of the solid as fixed degrees of freedom in x, y and z directions. For the fluid boundary conditions, the lateral nodes of the lower plate surface are defined as wall boundary condition (No-slip boundary condition).

The damping and stiffness coefficients are determined as follows: first the free eigenfrequencies and mode shapes of the structure are determined by performing a modal analysis of the solid structure. Next, for each resonance frequency, the eigenvectors are used to calculate the resulting pressure distribution which represents the acting force applied by the fluid at each mode. Therefore, ANSYS enables the computation of the squeeze stiffness and damping parameters.

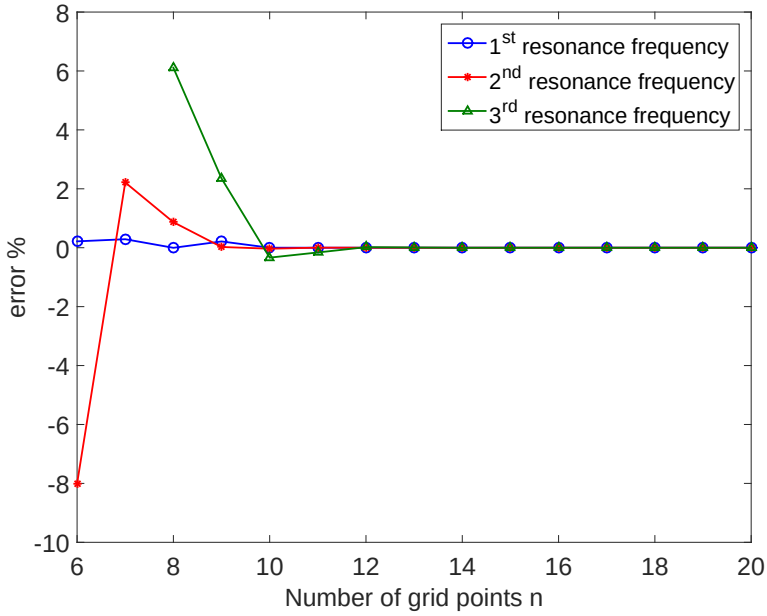

Figure 2: The convergence of the first three resonance frequencies for a pressure $P_0 = 1$ bar with respect to the number of grid points n

5. Parametric and comparative study

In this section, we compare the free resonance frequencies of the circular microplate coupled with the squeeze film model using the two methods outlined in the previous sections. For the two models, we suppose that the gap distance is uniform along the r axis by neglecting the thickness of the bottom electrode ($d_e = 0$ nm) and we choose a null electrostatic force ($V_{dc} = 0$ V) in order to investigate the effect of the film of air on the natural resonance frequencies of the plate. The number of grid points used in the reduced order model is $n = 20$. For the two models, the damping c is chosen to be negligible.

In Figure 4, the resonance frequencies and damping parameters of the first two modes are calculated using the two presented models while changing the pressure P_0. For low pressures ($P_0 = 10^{-2}$ Pa), the resonance frequencies are equal to the natural frequencies of a circular plate. In this case, the air film has no impact on the resonance frequencies and the error between the two models is less than 0.1%. By increasing the pressure in the gap until $P_0 = 10^3$ Pa, the natural frequencies remain almost unchanged. At this pressure, the resonance frequencies start to increase and the error between the FEM and DQM becomes notable. The pressure increase has a major impact on the Knudsen number which increases the squeeze parameter σ. For small squeeze number $\sigma << 1$, the air film can be treated as an incompressible fluid. However, for higher values of σ the fluid becomes compressible and leads to air-spring effect which results in a shift in the resonance frequencies. Also, the change in the gap pressure has an impact on the damping forces caused by the fluid. For low pressures, the damping forces are negligible and there is no interaction between the air and the microstructure. As we increase the pressure, the damping forces increase which

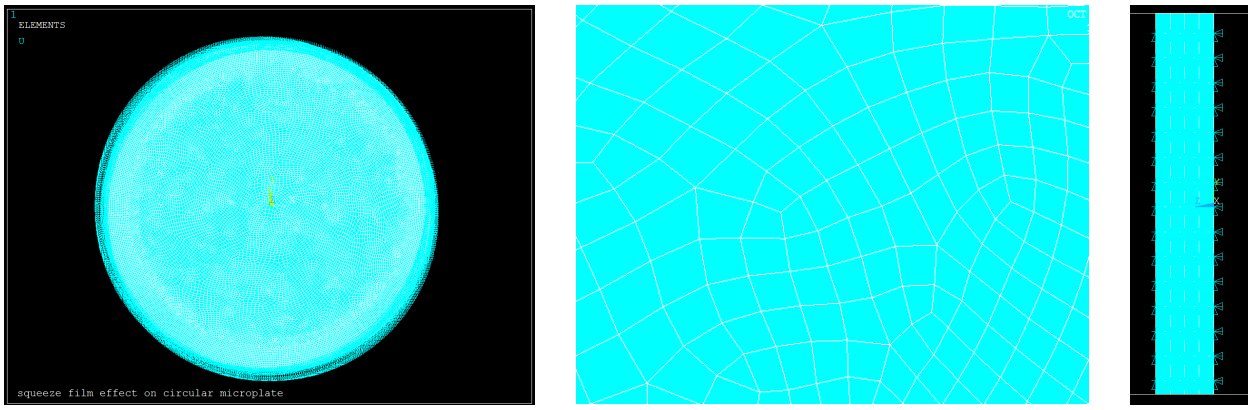

Figure 3: Front and side views of the clamped circular plate modeled in ANSYS.

decreases the vibration amplitude of the plate. The damping parameters of the first two modes increase in a linear way while increasing the pressure.

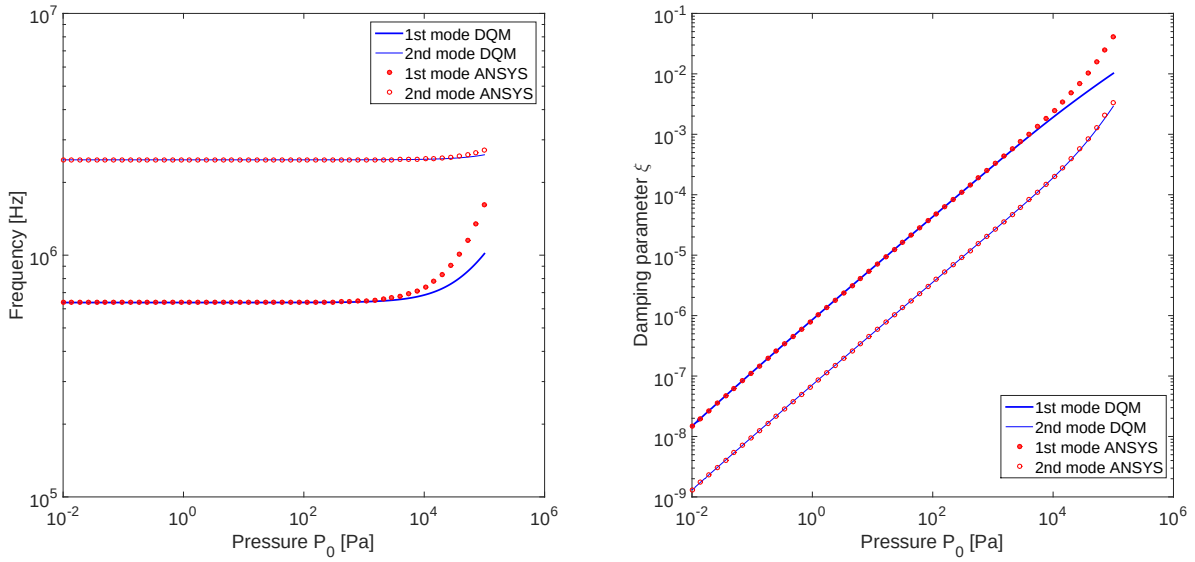

(a) (b)

Figure 4: The effect of changing the static pressure P_0 on (a) the resonance frequencies and (b) the damping coefficients for the first two axisymmetric modes.

In Figures 5 and 6, we respectively varied the parameters d and R at the atmospheric condition ($P_0 = 1bar$). In Figure 5, we display the resonance frequencies and the damping parameters of the coupled fluid-structure system. The squeeze number $\sigma = \frac{12\eta_{eff}R^2}{d^2P_0T}$ is proportional to $\frac{1}{d^2}$. For a small gap distance, the air film becomes very thin and the trapped air behaves as a spring which explains the shift in the resonance frequencies. At this level, the damping forces are negligible compared to the stiffness forces. The increase in the gap

distance leads to a decrease in the squeeze number σ. Hence, the damping forces increase and the stiffness forces decrease until they become equal at the cutoff squeeze number σ_c. Around this point the damping forces are maximal and the air behaves as a damper. By increasing more the gap distance, the damping and stiffness forces decrease and the air effects become negligible.

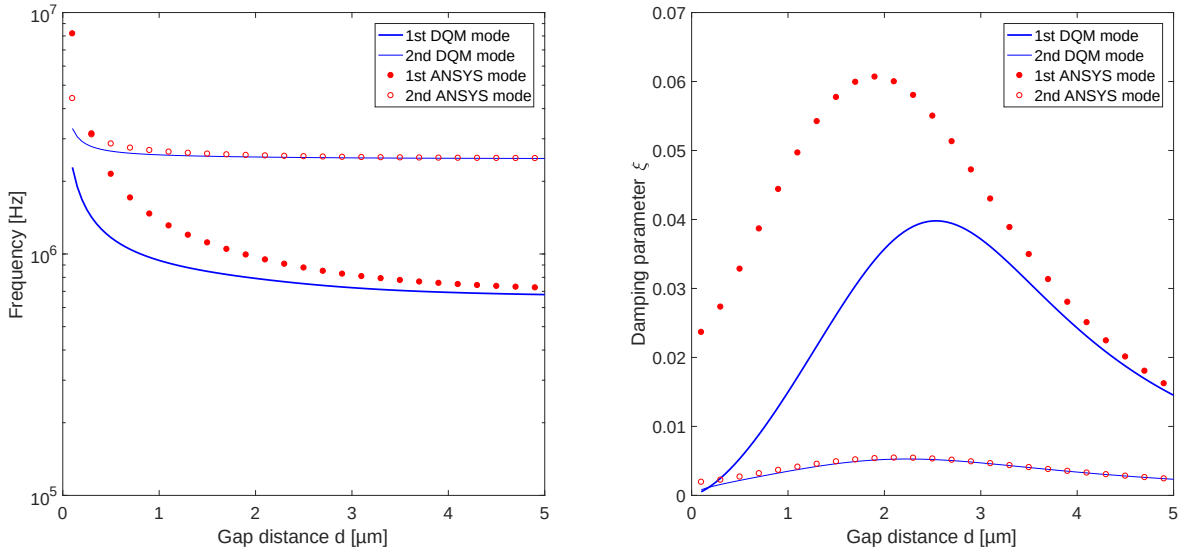

(a) (b)

Figure 5: The effect of changing the gap distance d on (a) the resonance frequencies and (b) the damping coefficients for the first two axisymmetric modes.

In Figure 6, we display the effect of changing the radius of the microplate on the resonance frequencies and damping parameters of the first two modes. As we know, the change in the radius of the plate changes the natural resonance frequencies. The squeeze number defined previously as:

$$\sigma = \frac{12\eta_{eff}R^2}{d^2P_0T} = \frac{12\eta_{eff}}{d^2P_0\sqrt{\frac{\rho h}{D}}} \tag{36}$$

is independent of the plate radius R. However, the nondimensional quantity $P_{ND} = \frac{R^4P_0}{Dd}$, which represents the impact of the pressure on the plate, is proportional to R^4. As shown in Figure 6, the damping forces increase with respect to the plate radius due to the increase in the surface of contact between the air and the plate. We can conclude that for a multiphysical problem, σ and P_{ND} are the two main nondimensional parameters that quantify the effect of the squeeze film on the dynamic behavior of the microplate.

In Figures 4, 5 and 6, we notice that for small value of σ and P_{ND}, the air film has a small effect on the dynamic behavior of the microplate and the numerical results determined using ANSYS and DQM are in good agreement. However, at higher values of σ and P_{ND} the error between the two methods increases. The FEM method is based on first solving the

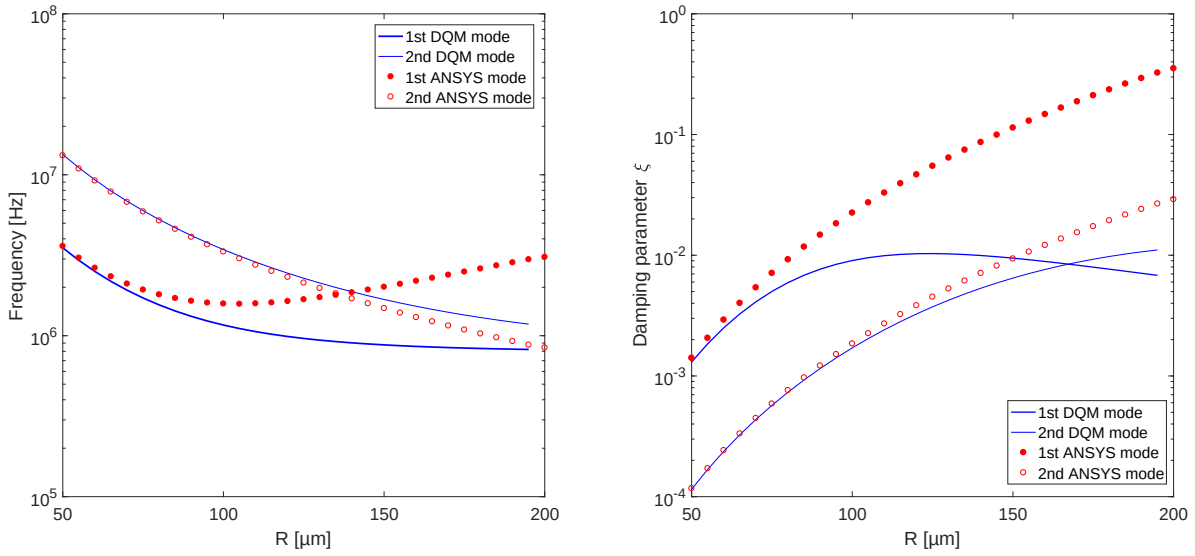

(a) (b)

Figure 6: The effect of changing the plate radius R on (a) the resonance frequencies and (b) the damping coefficients for the first two axisymmetric modes.

mechanical problem and implementing the obtained results into the Reynolds equation. The limitation of this method is that the eigenvalues and eigenvectors of the mechanical problem are not depending of the squeeze parameter σ. That means the squeeze effects are always determined at the natural resonance frequencies of the plate without taking into account the frequency shift caused by the Reynolds equation. In the case of the DQM, the eigenvalues and eigenvectors of the multiphysical problem are obtained by solving the coupled fluid and solid system of equations. Also, the finite element model defined in ANSYS is valid only in the case of small displacement ($w << 1$) and small pressure changes ($P << 1$). In Figures 4 and 5, the non dimensional parameter $\beta = \frac{d}{R}$ ranging between 10^{-3} and 5×10^{-2}. However, when β increases and becomes close to 1, Reynolds equation approaches its limit of validation.

Another feature of the DQM is that we can determine the mode shapes of the microplate and the pressure of the coupled problem. Several techniques have been presented in the literature on the determination of the mode shapes of a coupled problem. Nayfeh *et al.* [30] used the perturbation technique to solve the coupled problem and to approximate the mode shapes and the resonance frequencies. This method is efficient especially for a simple system such as a microbeam. However, the determination of the mode shapes for a two dimensional system is difficult. Another analytical approach was used by Darfing *et al.* [54] to determine the pressure mode shapes based on the Green's function. This method was used to determine the resulting squeeze film forces acting on a microplate. However, the mode shapes of the mechanical problem are determined independently of the Reynolds equation which makes this method only valid for a small squeeze number. The drawbacks of these

methods is that when we change the boundary conditions of the problem, the expression of the mode shape should be modified. In our case, the mode shape of the coupled problem can be easily determined for different configurations (clamped or free boundary conditions) and with different membrane shapes (circular, rectangular, hexagonal....). Unlike FEM, the determination of the mode shapes and squeeze effects using DQM requires only few grid points.

In Figure 7, we present the real and imaginary shape functions of a clamped circular microplate at atmospheric pressure. At $r = R$, a rigid wall boundary condition is imposed for the fluid . The mode shapes satisfy the boundary conditions (26). At the center of the membrane, the displacement and the pressure are maximal. Therefore, the mode shapes have a horizontal tangent at $r = 0$. For the clamped boundary conditions, the displacement at $r = R$ is null and the pressure satisfies the rigid wall boundary condition which represents a horizontal tangent.

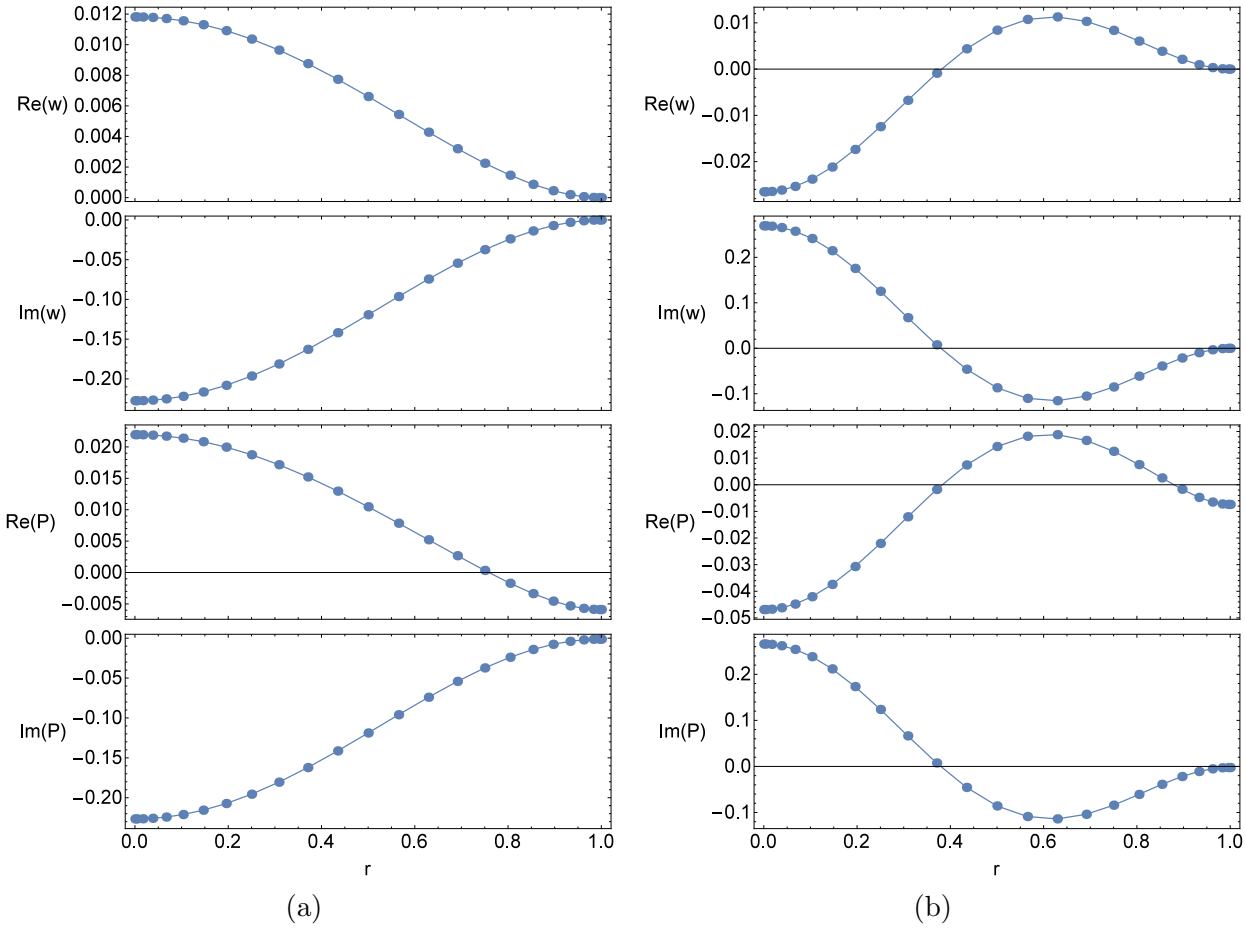

Figure 7: The real and imaginary eigenvectors of the first two axisymmetric modes for the solid and fluid at atmospheric pressure $P_0 = 1$ bar and for 25 grid points: (a) the first mode and (b) the second mode.

6. Experimental investigations of the squeeze film effects

The CMUT has been fabricated using a low-temperature fabrication technique based on anodic bonding of SOI wafer on a glass wafer [55]. The idea behind this method is to define the cavity and the membrane on different wafers and after that they are bonded in a vacuum condition. For the wafer bonding process, the membrane is a layer of silicon bonded on a glace Borofloat 33 wafer. this fabrication process is characterized by few fabrications steps than the sacrificial release technique [56, 57] which makes it shorter and faster for manufacturing. Also, The membrane is made of single-crystalline silicon layer with a good mechanical property, good thickness uniformity and low internal stress. These properties increase transduction efficiency of the CMUT in transmit and receive mode.

In the previous section, we assumed that the gap distance along the r axis is uniform. However, the electrode thickness can change the gap distance because when $r > R_e$, $H(t) = d + d_e - w(t)$ as displayed in Equation (10). This geometric parameter has been taken into account in the model.

For the experimental tests, the wafer is placed inside a vacuum chamber in order to eliminate the fluid interaction with the microsystem. As shown in Figure 8, two probes are placed inside the chamber to ensure the electric connections. The vacuum chamber has a transparent window (Plexiglas) that enables the laser beam to penetrate without any distortion. The DC and AC voltages are generated with a DC and AC generators. The two voltages are combined using a coupling circuit. The displacement/velocity are measured using a vibrometer OFV-534 (*Polytec*) at the center of the microplate. The decoder transforms the optical signal to an electrical one which will be displayed in the oscilloscope. The measured electrical signal is proportional to the vibration amplitude. The laser vibrometer is characterized by a high precision (can go up to 1 pm for the displacement and 10 m/s for the velocity) and a wide frequency range (up to 24 MHz) [58].

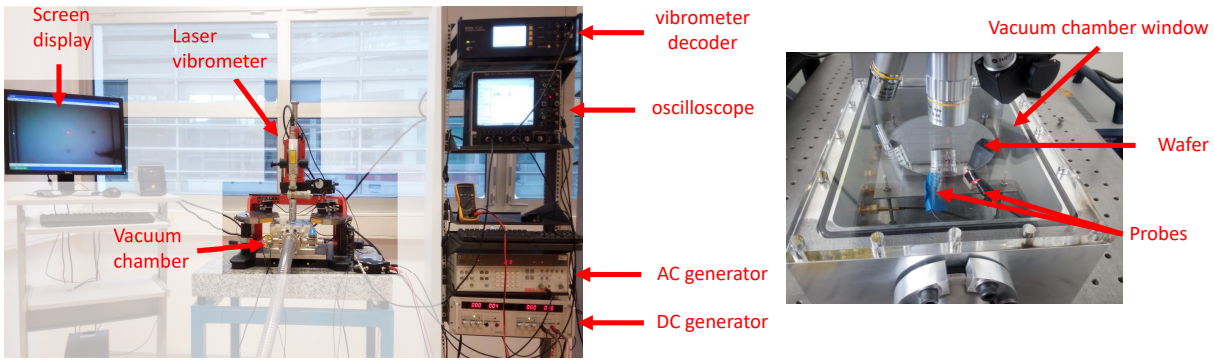

Figure 8: Experimental setup based on OFV-534 laser Doppler vibrometer used for the dynamic characterization of the microplate in term of frequency response.

In Figure 9, we compare the experimental and numerical resonance frequencies of the microplate at different pressures P_0. The microplate is actuated with a DC voltage combined with a periodic chirp signal with an amplitude V_{ac}. For low pressure ($P_0 = 0.45$ mbar), the resonance frequencies of the microsystem are equal to the natural resonance frequencies of

the microplate. At this pressure, the air effects on the solid are negligible. By increasing the pressure, the trapped air inside the gap behaves like a spring which explains the increase in the resonance frequencies.

Figure 9 shows that the numerical results obtained with the DQM approach are in good agreement with the experimental results even when the squeeze forces are important. The maximum error between the experimental and numerical results is less than 2.5 %. This error can be explained by the imperfect boundary conditions of the plate due to the apertures in the pad access (see Figure 1a). At vacuum, the resonance frequency of the microplate is equal to 610 kHz while it increases up to 973 kHz at atmospheric pressure. The difference in the resonance frequency is about 60 %. Therefore, the modeling of MEMS devices operating in atmospheric conditions should take into consideration the effect of fluid film.

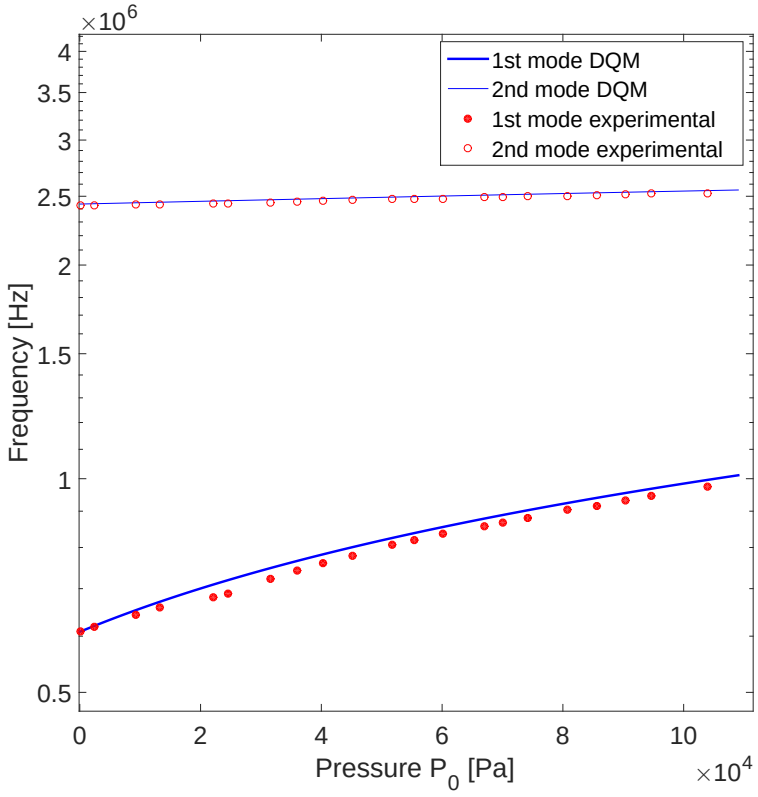

Figure 9: Experimental validation of the effect of the static pressure on the resonance frequencies.

Another major effect that is commonly studied in CMUTs is the DC voltage effect. The electrostatic force has a direct impact on the resonance frequencies. Figure 10 shows the variation of the first two resonance frequencies. As we increase the DC voltage, the fundamental natural frequency decreases until it reaches zero at a $V_{dc} = 34$ V (known as the pull-in voltage). The decrease in the resonance frequency is due to the negative stiffness caused by the electrostatic force. At pull-in voltage, the electrostatic force is equal to the restoring forces of the microplate.

Also, the DC voltage bends the microplate downward and decreases the gap distance which increases the effect of the squeeze film. In Figure 10, we present the resonance frequencies and the damping ratios of the first two axisymmetric modes for different DC voltages V_{dc} and pressures P_0. For a low pressure, the effect of the fluid film is negligible which explains the low damping and stiffness forces for the first two resonance frequencies. By increasing the pressure, the resonance frequencies shift upward due to the added stiffness caused by the air film. The change in the gap distance leads to an increase in the damping ratio of the first mode. For the second mode, the damping coefficient remains almost unchanged.

7. Nonlinear dynamics of a CMUT with squeeze film effects

7.1. Time response analysis

In this section, we investigate the nonlinear dynamic response of a CMUT by taking into account the squeeze film effects. Thus, the discretized system of equations (20)-(22) is solved using the long time integration method to determine the time response of the microplate. This method is based on the fourth order Runge-Kutta integration scheme. The simulations presented in this section were performed on a circular CMUT with the physical parameters presented in Table 1. The number of grid points used in simulations is $n = 8$.

Figure 11 depicts the time response of the microsystem forced with $V_{dc} = 30$ V and $V_{ac} = 1$ V at a nondimensional frequency $\omega = 13$. The microplate is simulated at atmospheric pressure condition . The time response in Figure 11(a) and (c) is composed of two regimes: transient and steady state. At the atmospheric pressure, the solution amplitude stabilizes rapidly due to the damping forces acting on the structure. As we showed in the previous section, the decrease in the gap pressure leads to a decrease in the damping forces which means the transient solution will take more time to stabilize.

As shown in Figure 11, the solution amplitude of the pressure is vibrating around a static solution however this is not the case when we perform experimental tests because the gap is not totally closed, due to an opening in the electrode pad (see Figure 1). Therefore, the static solution of P is always zero. When we choose the rigid wall as boundary condition for P, the static solution of $w(r, t)$ depends on the pressure in the gap. In Figure 12, we plot the effect of the static pressure P_0 on the static solution of the membrane displacement w and pressure P. First, we apply a DC voltage $V_{dc} = 30$ V to the microplate and we solve the system in time domain using Runge-Kutta method and we determine the static solution for w and P for different values of P_0. The initial conditions for these simulations are chosen to be zero for w and P ($w(t = 0) = 0$ and $P(t = 0) = 0$). As shown in Figure 12, for a low pressure P_0, the static pressure has a small effect on the static displacement and the total displacement is equal to the static displacement of the membrane, when we solve only the mechanical equations. However, as we increase the pressure P_0, the static solution changes and the total displacement decreases. This is due to the pressure difference between the upper and the lower surfaces of the microplate. At atmospheric pressure, the static solution decreases by 43 % which modifies the static pressure P_0. As the pressure increases the static

solution of P increases. The changes in the static solution of w and P have an important impact on the dynamic solution of the coupled problem.

From an experimental point of view, the static displacement does not depend on the pressure inside the gap. Therefore, the choice of rigid wall boundary condition for the fluid can generate an error in the static and dynamic tests. Also the dynamic solution of the microplate depends on the initial conditions chosen at $t = 0$. Hence, in the next section, we will choose the boundary as an open boundary condition for the fluid.

7.2. Frequency response analysis

In this section, we study the frequency response of the microplate forced with an AC voltage near the primary resonance frequency. We assume that the only damping source is coming from the air film. The boundary conditions of the microplate are chosen to be clamped for the solid and open for the fluid. Therefore, boundary conditions (26) become:

$$\begin{aligned}
&\text{At } \ r = 0: && \sum_{j=1}^{n} A_{1j}^{(1)} w_j = 0 && u_1 = 0 && \sum_{j=1}^{n} A_{1j}^{(1)} \bar{P}_j = 0 \\
&\text{At } \ r = 1: && \sum_{j=1}^{n} A_{nj}^{(1)} w_j = w_n = 0 && u_n = 0 && P_n = 0
\end{aligned} \tag{37}$$

For the periodic solution of the microplate, we use the finite difference method (FDM) to determine the microplate response when the stable region is reached [59, 60]. The period of the solution, with a frequency ω, is equal to $T_p = 2\pi/\omega$. First we discretize the period T_p into N_p time segments. Then, at each point, we write the first and second derivative of w_i using the centered difference approximation with fourth order error as:

$$\begin{aligned}
\dot{w}_i^k &= \frac{-w_i^{k+2} + 8w_i^{k+1} - 8w_i^{k-1} + w_i^{k-2}}{12\,(T_p/N_p)} \\
\dot{P}_i^k &= \frac{-P_i^{k+2} + 8P_i^{k+1} - 8P_i^{k-1} + P_i^{k-2}}{12\,(T_p/N_p)} \\
\ddot{w}_i^k &= \frac{-w_i^{k+2} + 16w_i^{k+1} - 30w_i^k + 16w_i^{k-1} - w_i^{k-2}}{12(T_p/N_p)^2}
\end{aligned} \tag{38}$$

where w_i^k is the displacement of the ith grid point at $t = k/N_p$. At the boundary time conditions:

$$\begin{aligned}
w_i^k &= w_i^{N_p+k} && \text{and} && P_i^k = P_i^{N_p+k} && \text{if} && k \leq 0 \\
w_i^k &= w_i^{k-N_p} && \text{and} && P_i^k = P_i^{k-N_p} && \text{if} && k > N_p
\end{aligned} \tag{39}$$

As we presented in section 4.1, the nonlinear coupled differential equations (20) and (22) is a $2 \times n - 5$ ordinary differential equations and each of these ODE is descretized

into N_p algebraic equations using FDM which makes the total equations to solve equal to $(2 \times n - 5) \times N_p$.

FDM is coupled with the arclength continuation method to determine how the solution of a system varies with respect to a certain parameter [59]. We consider the following algebraic system:

$$F(X, \alpha) = 0 \tag{40}$$

where α is the continuation parameter and X is the unknown parameter. The idea of this method is to avoid varying the parameter α by parametrizing the variables X and α via a new continuation parameter s, $X = X(s)$ and $\alpha = \alpha(s)$. The system of equations becomes:

$$F(X(s), \alpha(s)) = 0 \tag{41}$$

To solve this system of equations, we add an additional equation specified by Euclidean arclength normalization [59].

$$X^T X + \alpha^2 = 1 \tag{42}$$

where the initial conditions for (41) and (42) are given by

$$X(0) = X_0 \qquad \text{and} \qquad \alpha(0) = \alpha_0 \tag{43}$$

The nonlinear coupled algebraic equations (20) and (22) are solved using the FDM coupled with the arclength continuation technique, where

$$F(X(s), \alpha(s)) = \begin{cases} EQ_w^{dy}(w_i^k(s), u_i^k(s), P_i^k(s)) & i = 2, \cdots, n-2; k = 1, \cdots, N_p \\ EQ_P^{dy}(w_i^k(s), P_i^k(s)) & i = 2, \cdots, n-1; k = 1, \cdots, N_p \end{cases} \tag{44}$$

where the vector of unknowns is:

$$X(s) = \left\{ w_i^k(s), P_j^k(s) \right\} \qquad i = 2, \cdots, n-2;\ j = 2, \cdots, n-1 \text{ and } k = 1, \cdots, N_p \tag{45}$$

where n is the number of grid points, N_P is the number of segments in the periodic solution and $\alpha = \omega$ is the control parameter .

In Figure 13, we present the frequency response of the microplate for several pressures P_0. The microplate is actuated with a DC voltage $V_{dc} = 31$ V and an AC voltage $V_{ac} = 1$ V. At atmospheric pressure, the frequency response of the microplate is linear and this is due to the damping added by the squeeze model. The decrease in the pressure P_0 inside the gap has two effects on the dynamic behavior of the CMUT: first, it shifts the resonance frequency and second it increases the vibration amplitude. In fact, the decrease of the pressure in the medium reduces the stiffness and the damping effects caused by the air film. Figure 13(a) shows the maximum displacement at the center of the microplate. By decreasing the static pressure P_0, the frequency response of the microplate starts to bend to the left and exhibits a softening effect. For high DC voltages, the electrostatic nonlinearity is dominant over the geometric nonlinearity. In Figure 13(b), we display the variation of the maximum net pressure $P(t)$ with respect to the excitation frequency. Despite the decrease of the pressure

P_0 in the gap, the maximum pressure $P(t)$ increases due to the increase in the vibration amplitude $w(t)$.

In Figure 14, we simulate the frequency response of the CMUT at atmospheric condition for different AC voltages and for $V_{dc} = 15$ V. The increase in the AC voltage leads to an increase in the vibration amplitude without a change in the resonance frequency. In Figure 14(a), we display the maximum displacement of the microplate center with respect to the resonance frequency. At a low AC voltage, the frequency response of the microplate is linear. However, by increasing the AC voltage the frequency response becomes nonlinear and exhibits a hardening behavior beyond the critical amplitude [61, 62, 63]. For instance, when the AC voltage $V_{ac} = 15$ V, the curve is tilted to the right and multiple solutions are obtained. In Figure 14(b), we display the effect of AC voltage on the dimensional pressure $P(t)$. Due to the increase in the vibration amplitude, the relative pressure increases and becomes nonlinear for $V_{ac} = 15$ V. Actuating the CMUT with high voltage is very important for several application such as High-intensity focused ultrasound (HIFU) and our model can predict the nonlinear behavior of the CMUT operating in atmospheric conditions.

7.3. Force response analysis

In this section, we study the effect of the pressure P_0 on the force response curves of the CMUT. In Figure 15, we simulate the maximum amplitude and pressure at the center of the microplate with respect to the forcing voltage V_{ac} and for several pressures P_0. The microplate is actuated with a DC voltage $V_{dc} = 31$ V at a constant frequency 700 KHz. For this DC voltage the microplate has a softening type behavior (see Figure 13). There are two bifurcation points with unstable branch in between and two stable solutions. For $V_{ac} = 0$ V, the maximum displacement of the membrane is equal to the static solution when the membrane is forced with a DC voltage $V_{dc} = 31$ V. By increasing the pressure in the gap, the voltage of the first bifurcation point strongly increases, whereas the second bifurcation point slightly increases and this increases the bistability domain in the force response curves. For this configuration, the air film is behaving as a spring. In fact, an increase in the pressure leads to a shift in the resonance frequency, while the damping force is slightly changed, which is illustrated in Figure 4. Therefore, to reach the first limit point, high actuation voltages are required for high pressure P_0.

8. Conclusion

In this paper, we have developed a nonlinear model for a circular microplate by taking into account the squeeze film effects. The pressure distribution inside the gap has been modeled using the Reynolds equation. The validity region of the Reynolds equation is extended by replacing the viscosity of the fluid with an effective one using the Veijola model. The coupled differential equations, solid and fluid, have been discretized with DQM using the same grid points for the solid and fluid. The resonance frequencies and the damping coefficients of the multiphysical problem are determined by solving the linear damped system. Another method was also presented, which is based on FEM model implemsented in ANSYS. The two models showed a good agreement especially for a low squeeze number. For

low pressure P_0, the damping and stiffness forces of the air film are negligible and by increasing the pressure, the resonance frequencies shift and the damping force increases. Several simulations were also performed for different design parameters R and d. The squeeze film effects depend mainly on the squeeze number σ. The advantage of DQM is that we can determine the complex eigenvectors and eigenvalues of the solid and fluid. Also, it provides more accurate results than ANSYS model because for this type of FEM model, the squeeze forces are determined at the natural resonance frequencies of the microplate without taking into account the shift in the resonance frequencies caused by the fluid. Our model has been also validated with respect to experimental results for different static pressures.

We have also studied the nonlinear dynamic behavior of the microplate under the squeeze film effects. The fluid can have two possible boundary conditions: *(i)* closed boundary condition for which the relative pressure P has a static solution that can change the static displacement of the microplate and the time response strongly depends on the initial conditions of the solid and fluid at $t = 0$, *(ii)* open boundary condition which is relatively consistent with the fabricated device due to the pad channel.

For open boundary condition, we have plotted the frequency responses of the CMUT at different pressures P_0 using DQM. It has been shown that the decrease in the pressure leads to an increase in the vibration amplitude, a shift in the resonance frequency and a nonlinear behavior of the microsystem. At atmospheric pressure, the nonlinear regime can be reached by applying high DC and AC voltages to conquer the damping force. In the force response curves, the increase in the pressure leads to an increase in the bistability region.

The proposed approach is very efficient in predicting the nonlinear behavior of capacitive resonators, such as CMUT, operating in atmospheric conditions. This model can be exploited by MEMS designers in order to enhance the performances of CMUTs, enabling the generation of acoustic waves with high intensity.

Acknowledgements

This project has been performed in cooperation with the EIPHI Graduate School (contract "ANR-17-EURE-0002").

References

[1] W. E. Newell, Miniaturization of tuning forks, Science 161 (3848) (1968) 1320–1326.

[2] R. J. Dolleman, D. Davidovikj, S. J. Cartamil-Bueno, H. S. van der Zant, P. G. Steeneken, Graphene squeeze-film pressure sensors, Nano letters 16 (1) (2015) 568–571.

[3] O. Reynolds, On the theory of lubrication and its application to mr. beauchamp tower's experiments, including an experimental determination of the viscosity of olive oil., Proceedings of the Royal Society of London 40 (242-245) (1886) 191–203.

[4] E. Salbu, Compressible squeeze films and squeeze bearings, Journal of Basic Engineering 86 (2) (1964) 355–364.

[5] S. Hutcherson, W. Ye, On the squeeze-film damping of micro-resonators in the free-molecule regime, Journal of Micromechanics and Microengineering 14 (12) (2004) 1726.

[6] Y.-T. Hsia, G. Domoto, An experimental investigation of molecular rarefaction effects in gas lubricated bearings at ultra-low clearances, Journal of Lubrication Technology 105 (1) (1983) 120–129.

[7] H. Seidel, H. Riedel, R. Kolbeck, G. Mück, W. Kupke, M. Königer, Capacitive silicon accelerometer with highly symmetrical design, Sensors and Actuators A: Physical 21 (1-3) (1990) 312–315.

[8] Y. Mitsuya, Modified reynolds equation for ultra-thin film gas lubrication using 1.5-order slip-flow model and considering surface accommodation coefficient, Transactions-American Society of Mechanical Engineers journal of tribology 115 (1993) 289–289.

[9] M. Andrews, I. Harris, G. Turner, A comparison of squeeze-film theory with measurements on a microstructure, Sensors and actuators A: physical 36 (1) (1993) 79–87.

[10] T. Veijola, H. Kuisma, J. Lahdenperä, T. Ryhänen, Equivalent-circuit model of the squeezed gas film in a silicon accelerometer, Sensors and Actuators A: Physical 48 (3) (1995) 239–248.

[11] T. Veijola, A. Pursula, P. Råback, Extending the validity of squeezed-film damper models with elongations of surface dimensions, Journal of Micromechanics and Microengineering 15 (9) (2005) 1624.

[12] G. Schrag, G. Wachutka, Physically based modeling of squeeze film damping by mixed-level system simulation, Sensors and Actuators A: Physical 97 (2002) 193–200.

[13] G. De Pasquale, A. Somà, An energetic approach for the experimental identification of damping in microstructures, Mechanical Systems and Signal Processing 50 (2015) 338–348.

[14] W. U. Syed, A. Brimmo, O. Waheed, A. Bojesomo, M. H. Ali, I. Ocak, S. Chengliang, A. Chatterjee, I. A. M. Elfadel, Numerical modeling and validation of squeezed-film damping in vacuum-packaged industrial mems, J. Micromech. Microeng 27 (075016) (2017) 075016.

[15] H. Moeenfard, Analytical modeling of squeeze film damping in dual axis torsion microactuators, Surface Review and Letters 22 (01) (2015) 1550006.

[16] A. K. Pandey, R. Pratap, A semi-analytical model for squeeze-film damping including rarefaction in a mems torsion mirror with complex geometry, Journal of Micromechanics and Microengineering 18 (10) (2008) 105003.

[17] Z. Kádár, W. Kindt, A. Bossche, J. Mollinger, Quality factor of torsional resonators in the low-pressure region, Sensors and Actuators A: Physical 53 (1-3) (1996) 299–303.

[18] B. Li, H. Wu, C. Zhu, J. Liu, The theoretical analysis on damping characteristics of resonant microbeam in vacuum, Sensors and Actuators A: Physical 77 (3) (1999) 191–194.

[19] R. Christian, The theory of oscillating-vane vacuum gauges, Vacuum 16 (4) (1966) 175–178.

[20] M. Bao, H. Yang, H. Yin, Y. Sun, Energy transfer model for squeeze-film air damping in low vacuum, Journal of Micromechanics and Microengineering 12 (3) (2002) 341.

[21] S. Krylov, R. Maimon, Pull-in dynamics of an elastic beam actuated by continuously distributed electrostatic force, Journal of vibration and acoustics 126 (3) (2004) 332–342.

[22] S. Krylov, Lyapunov exponents as a criterion for the dynamic pull-in instability of electrostatically actuated microstructures, International Journal of Non-Linear Mechanics 42 (4) (2007) 626–642.

[23] H. M. Sedighi, A. Koochi, F. Daneshmand, M. Abadyan, Non-linear dynamic instability of a double-sided nano-bridge considering centrifugal force and rarefied gas flow, International Journal of Non-Linear Mechanics 77 (2015) 96–106.

[24] L.-D. Liao, P. C. Chao, C.-W. Huang, C.-W. Chiu, Dc dynamic and static pull-in predictions and anal-

ysis for electrostatically actuated clamped circular micro-plates based on a continuous model, Journal of Micromechanics and Microengineering 20 (2) (2009) 025013.
[25] S. Chaterjee, G. Pohit, Squeeze-film damping characteristics of cantilever microresonators for higher modes of flexural vibration, International Journal of Engineering, Science and Technology 2 (4) (2010) 187–199.
[26] T. Veijola, T. Mattila, Compact squeezed-film damping model for perforated surface, in: Transducers 01 Eurosensors XV, Springer, 2001, pp. 1478–1481.
[27] D. Homentcovschi, R. Miles, Viscous damping of perforated planar micromechanical structures, Sensors and Actuators A: Physical 119 (2) (2005) 544–552.
[28] Y. Fang, P. Li, F. Yang, W. Zuo, Squeeze-film damping of circular microplates vibrating in a tilting motion, Microfluidics and Nanofluidics 20 (11) (2016) 152.
[29] A. Ishfaque, B. Kim, Analytical solution for squeeze film damping of mems perforated circular plates using greens function, Nonlinear Dynamics 87 (3) (2017) 1603–1616.
[30] A. H. Nayfeh, M. I. Younis, A new approach to the modeling and simulation of flexible microstructures under the effect of squeeze-film damping, Journal of Micromechanics and Microengineering 14 (2) (2003) 170.
[31] M. I. Younis, Modeling and simulation of microelectromechanical systems in multi-physics fields, Ph.D. thesis (2004).
[32] R. Legtenberg, H. A. Tilmans, Electrostatically driven vacuum-encapsulated polysilicon resonators part i. design and fabrication, Sensors and actuators A: Physical 45 (1) (1994) 57–66.
[33] H. M. Ouakad, H. M. Al-Qahtani, M. A. Hawwa, Influence of squeeze-film damping on the dynamic behavior of a curved micro-beam, Advances in Mechanical Engineering 8 (6) (2016) 1687814016650120.
[34] G. W. Vogl, A. H. Nayfeh, A reduced-order model for electrically actuated clamped circular plates, Journal of Micromechanics and Microengineering 15 (4) (2005) 684.
[35] G. W. Vogl, A. H. Nayfeh, Primary resonance excitation of electrically actuated clamped circular plates, Nonlinear Dynamics 47 (1) (2007) 181–192.
[36] A. Jallouli, N. Kacem, G. Bourbon, P. Le Moal, V. Walter, J. Lardies, Pull-in instability tuning in imperfect nonlinear circular microplates under electrostatic actuation, Physics Letters A 380 (46) (2016) 3886–3890.
[37] N. Apte, K. K. Park, B. T. Khuri-Yakub, Finite element analysis of cmuts with pressurized cavities, in: Ultrasonics Symposium (IUS), 2012 IEEE International, IEEE, 2012, pp. 979–982.
[38] M. H. Ghayesh, H. Farokhi, Nonlinear behaviour of electrically actuated microplate-based mems resonators, Mechanical Systems and Signal Processing 109 (2018) 220–234.
[39] A. Jallouli, N. Kacem, J. Lardies, Investigations of the effects of geometric imperfections on the nonlinear static and dynamic behavior of capacitive micomachined ultrasonic transducers, Micromachines 9 (11) (2018) 575.
[40] A. Galisultanov, P. Le Moal, G. Bourbon, V. Walter, Squeeze film damping and stiffening in circular cmut with air-filled cavity: Influence of the lateral venting boundary conditions and the bias voltage, Sensors and Actuators A: Physical 266 (2017) 15–23.
[41] F. Najar, S. Choura, S. El-Borgi, E. Abdel-Rahman, A. Nayfeh, Modeling and design of variable-geometry electrostatic microactuators, Journal of micromechanics and microengineering 15 (3) (2004) 419.
[42] F. Najar, S. Choura, E. M. Abdel-Rahman, S. El-Borgi, A. Nayfeh, Dynamic analysis of variable-geometry electrostatic microactuators, Journal of micromechanics and microengineering 16 (11) (2006) 2449.
[43] E. Ventsel, T. Krauthammer, Thin plates and shells: theory: analysis, and applications, CRC press, 2001.
[44] S. D. Senturia, Microsystem design, Springer Science & Business Media, 2007.
[45] C. W. Bert, M. Malik, Semianalytical differential quadrature solution for free vibration analysis of rectangular plates, AIAA journal 34 (3) (1996) 601–606.
[46] J. Quan, C. Chang, New insights in solving distributed system equations by the quadrature methodi.

analysis, Computers & Chemical Engineering 13 (7) (1989) 779–788.
[47] C. Shu, B. Richard, Parallel simulation of incompressible viscous flows by generalized differential quadrature, Computing Systems in Engineering 3 (1-4) (1992) 271–281.
[48] C. Shu, B. E. Richards, Application of generalized differential quadrature to solve two-dimensional incompressible navier-stokes equations, International Journal for Numerical Methods in Fluids 15 (7) (1992) 791–798.
[49] J. R. Weaver, Centrosymmetric (cross-symmetric) matrices, their basic properties, eigenvalues, and eigenvectors, The American Mathematical Monthly 92 (10) (1985) 711–717.
[50] W. Chen, Y. Yu, X. Wang, Reducing the computational requirements of the differential quadrature method, Numerical Methods for Partial Differential Equations 12 (5).
[51] L. Meirovitch, Computational methods in structural dynamics, Vol. 5, Springer Science & Business Media, 1980.
[52] S. Saghir, S. Ilyas, N. Jaber, M. I. Younis, An experimental and theoretical investigation of the mechanical behavior of multilayer initially curved microplates under electrostatic actuation, Journal of Vibration and Acoustics 139 (4) (2017) 040901.
[53] A. M. A. Coupled-Field, Analysis guide.
[54] R. B. Darling, C. Hivick, J. Xu, Compact analytical modeling of squeeze film damping with arbitrary venting conditions using a green's function approach, Sensors and Actuators A: Physical 70 (1) (1998) 32–41.
[55] M. Bellaredj, G. Bourbon, V. Walter, P. Le Moal, M. Berthillier, Anodic bonding using soi wafer for fabrication of capacitive micromachined ultrasonic transducers, Journal of Micromechanics and Microengineering 24 (2) (2014) 025009.
[56] M. Haller, B. Khuri-Yakub, A surface micromachined electrostatic ultrasonic air transducer, in: Ultrasonics Symposium, 1994. Proceedings., 1994 IEEE, Vol. 2, IEEE, 1994, pp. 1241–1244.
[57] M. I. Haller, B. T. Khuri-Yakub, A surface micromachined electrostatic ultrasonic air transducer, IEEE Transactions on Ultrasonics, Ferroelectrics, and Frequency Control 43 (1) (1996) 1–6.
[58] E. Lawrence, Optical measurement techniques for dynamic characterization of mems devices, Polytec, Inc.
[59] A. H. Nayfeh, B. Balachandran, Applied nonlinear dynamics: analytical, computational and experimental methods, John Wiley & Sons, 2008.
[60] F. Najar, A. H. Nayfeh, E. M. Abdel-Rahman, S. Choura, S. El-Borgi, Dynamics and global stability of beam-based electrostatic microactuators, Journal of Vibration and Control 16 (5) (2010) 721–748.
[61] N. Kacem, S. Hentz, D. Pinto, B. Reig, V. Nguyen, Nonlinear dynamics of nanomechanical beam resonators: improving the performance of nems-based sensors, Nanotechnology 20 (27) (2009) 275501.
[62] N. Kacem, J. Arcamone, F. Perez-Murano, S. Hentz, Dynamic range enhancement of nonlinear nanomechanical resonant cantilevers for highly sensitive nems gas/mass sensor applications, Journal of Micromechanics and Microengineering 20 (4) (2010) 045023.
[63] N. Kacem, S. Hentz, S. Baguet, R. Dufour, Forced large amplitude periodic vibrations of non-linear mathieu resonators for microgyroscope applications, International Journal of Non-Linear Mechanics 46 (10) (2011) 1347–1355.

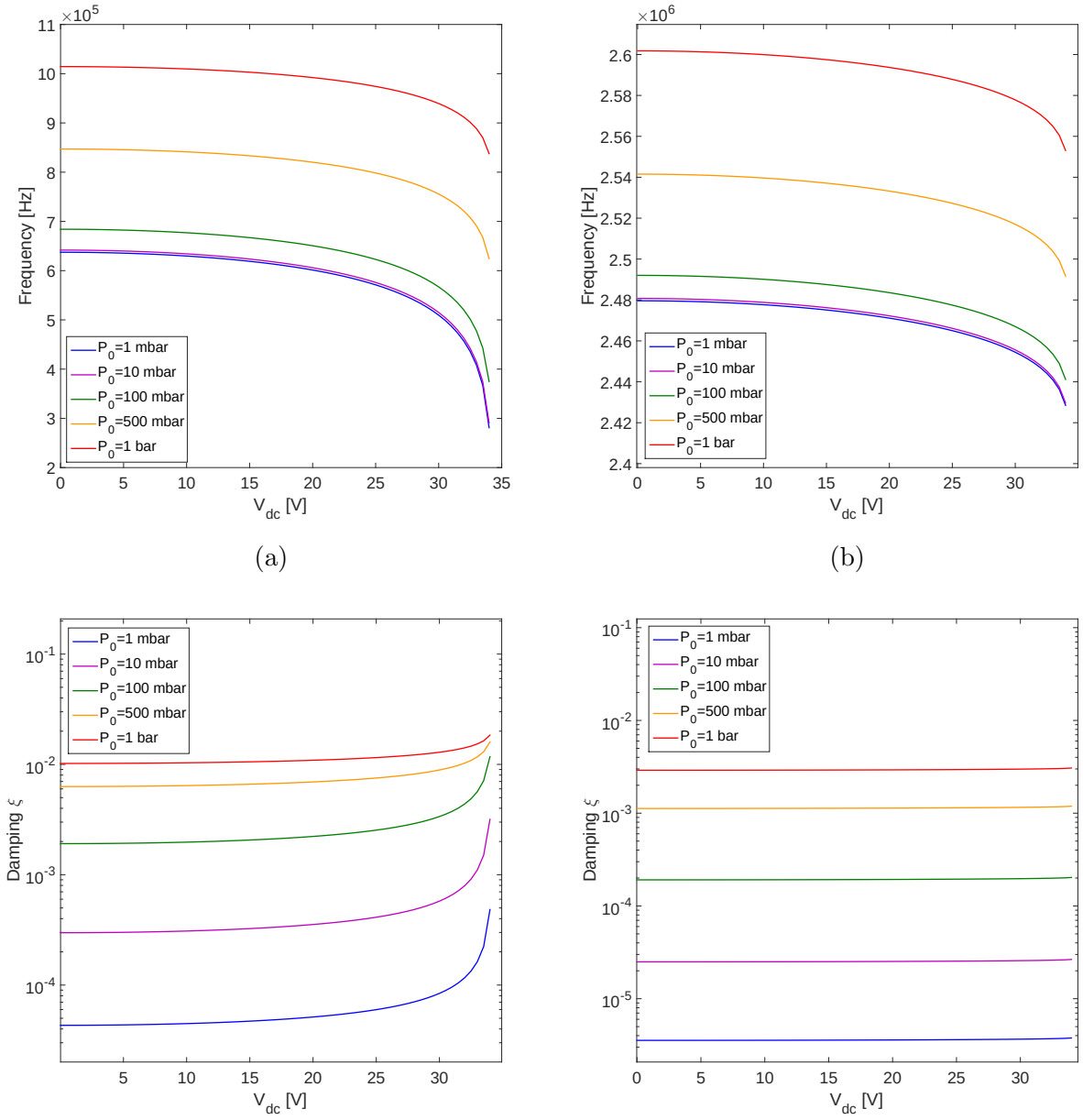

Figure 10: The effect of the DC voltage on the resonance frequencies and damping coefficients for several pressures P_0: (a) and (c) the first axisymmetric mode, (b) and (d) the second axisymmetric mode.

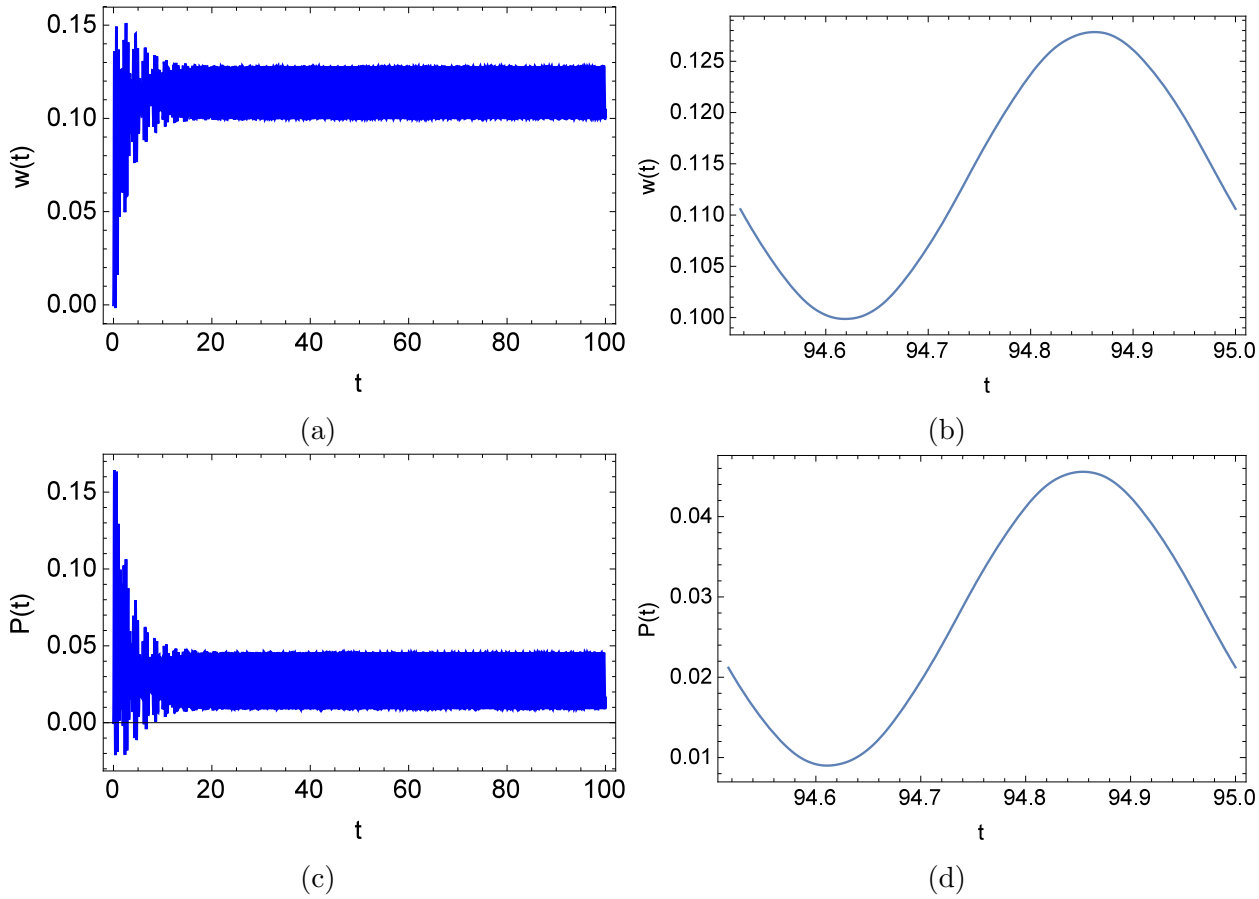

Figure 11: Time response of the microplate for $V_{dc} = 30$ V, $V_{ac} = 1$ V, $P_0 = 1$ bar at the dimensionless frequency $\omega = 13$ with the physical parameters defined in Table 1: (a) time response of $w(t)$, (b) the steady state solution of $w(t)$, (c) time response of $P(t)$, (d) the steady state solution of $P(t)$.

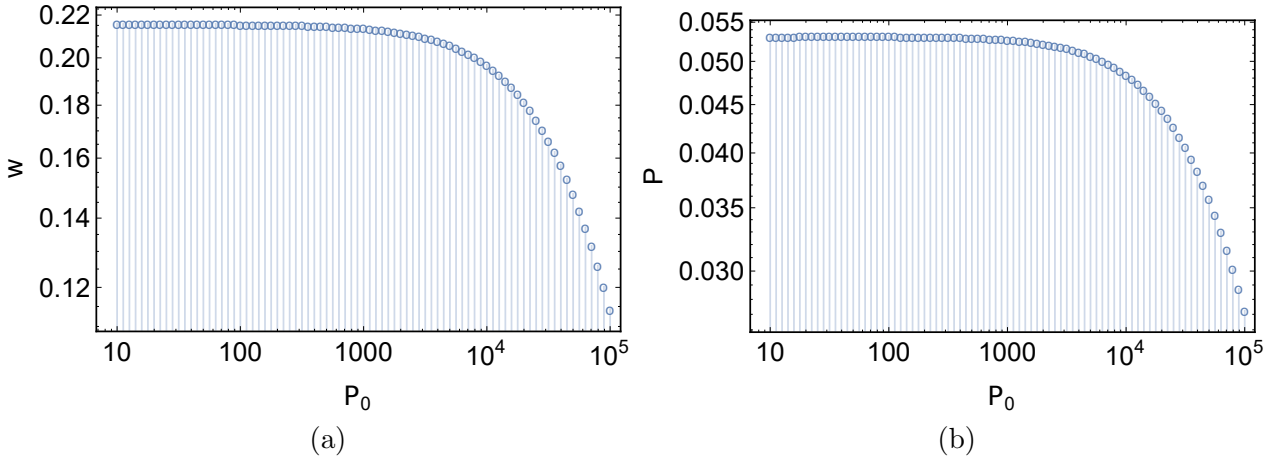

Figure 12: Dimensionless static response of w and P for several static pressures P_0 and $V_{dc} = 30$ V. The static solution is determined at the center of the microplate using the Runge-Kutta method and for the initial conditions $w(t = 0) = 0$ and $P(t = 0) = 0$.

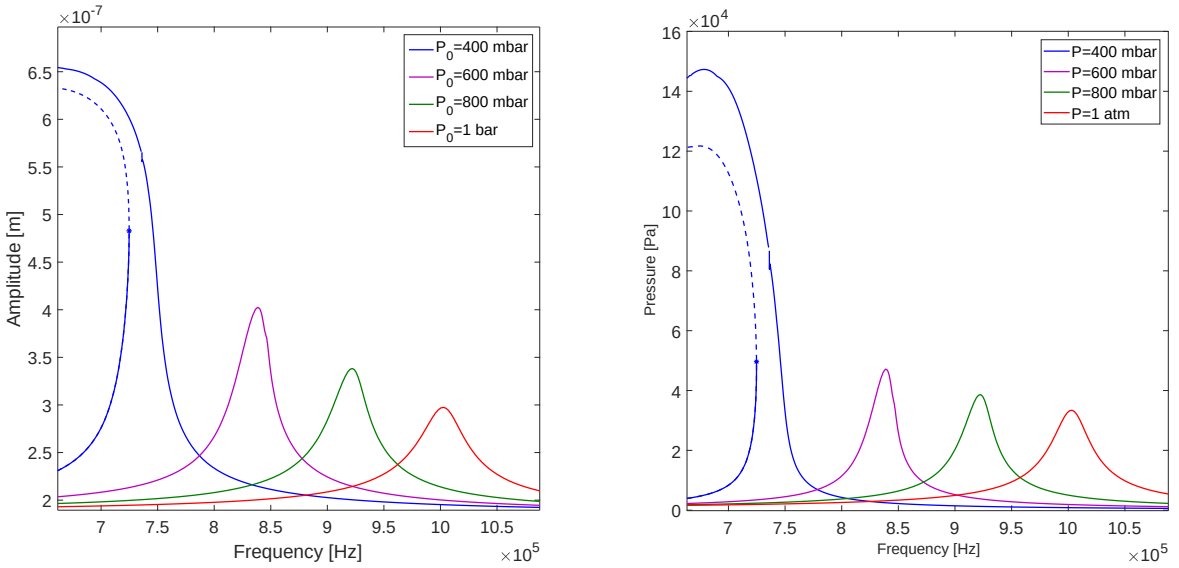

(a) (b)

Figure 13: Frequency responses of (a) $w(t)$ and (b) $P(t)$ for $V_{dc} = 31$ V and $V_{ac} = 1$ V, at the center of the microplate for several static pressures P_0. The physical parameters used in the simulations are defined in Table 1. The solid and dashed lines represent the stable and unstable solutions respectively and the star (*) represents the bifurcation point.

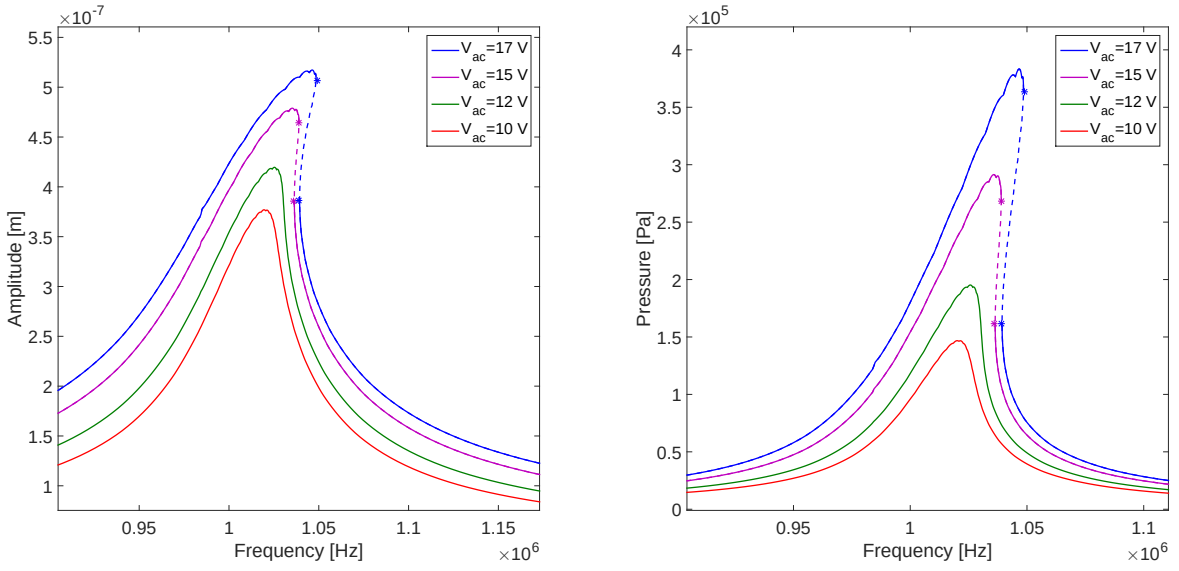

(a) (b)

Figure 14: Frequency responses of (a) $w(t)$ and (b) $P(t)$ for $V_{dc} = 15$ V and $P_0 = 1$ bar, at the center of the microplate for several voltages V_{ac}. The physical parameters used in the simulations are defined in Table 1. The solid and dashed lines represent the stable and unstable solutions respectively and the star (*) represents the bifurcation point.

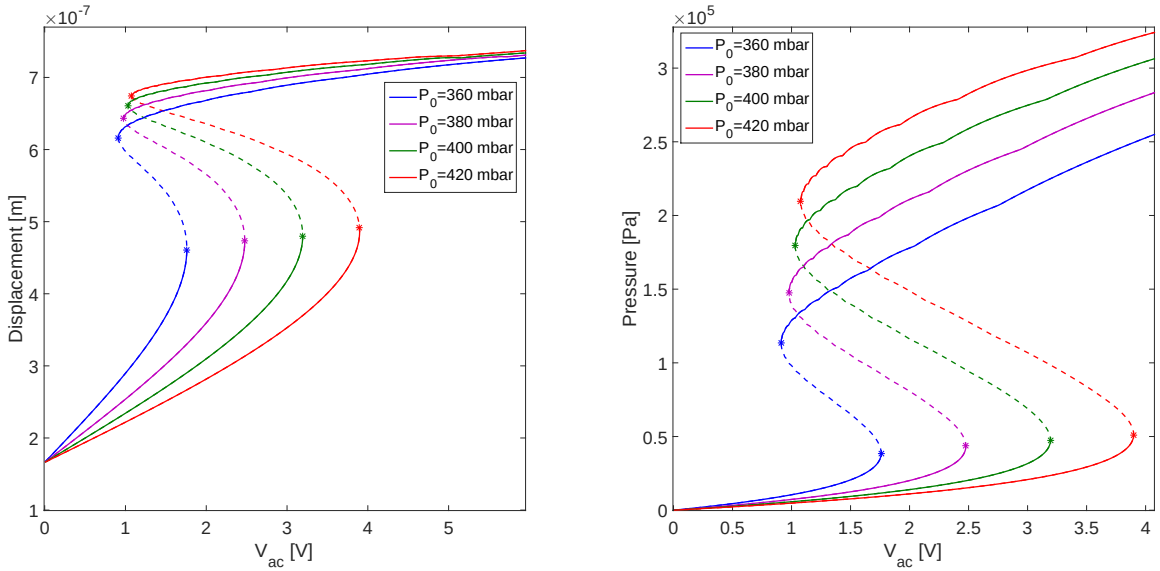

(a) (b)

Figure 15: Force responses of the maximum displacement and pressure at the center of the microplate, for $V_{dc} = 31$ V and at the frequency 700 KHz. The physical parameters used in the simulations are defined in Table 1. The solid and dashed lines represent the stable and unstable solutions respectively and the star (*) represents the bifurcation point.